

Review

# Nanocomposites of Ferrites with TiO<sub>2</sub>, SiO<sub>2</sub> and Carbon Quantum Dots as Photocatalysts for Degradation of Organic Pollutants and Microbes

Ajaypal Kaur<sup>1</sup>, Manpreet Kaur<sup>1,\*</sup> , Vasundhara Singh<sup>2</sup> and Pratibha Vyas<sup>3</sup> 

<sup>1</sup> Department of Chemistry, Punjab Agricultural University, Ludhiana 141004, India; ghumanajaypal94@gmail.com

<sup>2</sup> Department of Applied Science, Punjab Engineering College, Chandigarh 160012, India; vasundhara@pec.ac.in

<sup>3</sup> Department of Microbiology, Punjab Agricultural University, Ludhiana 141004, India; vyasp2000@pau.edu

\* Correspondence: manpreetchem@pau.edu

**Abstract:** Ferrites are important magnetic materials used in electronic devices. Nanocomposites of ferrites with TiO<sub>2</sub>, SiO<sub>2</sub> and carbon quantum dots have gained recent interest due to their unique advantages, such as high chemical stability, surface-active sites, high specific surface area, non-toxicity, excellent optical properties, and tunable porosity. In the present review, general and adaptable coprecipitation, sol–gel, hydrothermal, solvothermal, and Stöber methods for the fabrication of nanocomposites are discussed. These materials offer the advantage of magnetic recovery and superior photocatalytic performance. The potential of nanocomposites to act as photocatalysts to eliminate organic pollutants and microbes from water is discussed. Mechanisms involved in these applications are also elaborated upon. The review provides a detailed study of recent applications and future perspectives of nanocomposites in sustainable water treatment.

**Keywords:** ferrites; TiO<sub>2</sub>; SiO<sub>2</sub>; carbon quantum dots; nanocomposites; photocatalysis



**Citation:** Kaur, A.; Kaur, M.; Singh, V.; Vyas, P. Nanocomposites of Ferrites with TiO<sub>2</sub>, SiO<sub>2</sub> and Carbon Quantum Dots as Photocatalysts for Degradation of Organic Pollutants and Microbes. *Magnetochemistry* **2023**, *9*, 127. <https://doi.org/10.3390/magnetochemistry9050127>

Academic Editor: Huaili Zheng

Received: 7 April 2023

Revised: 2 May 2023

Accepted: 7 May 2023

Published: 9 May 2023



**Copyright:** © 2023 by the authors. Licensee MDPI, Basel, Switzerland. This article is an open access article distributed under the terms and conditions of the Creative Commons Attribution (CC BY) license (<https://creativecommons.org/licenses/by/4.0/>).

## 1. Introduction

For the environment and human life, developing industrialization has been both beneficial and problematic. Many harmful compounds, such as synthetic dyes, heavy-metal ions, and pesticides as well as microorganisms can degrade the quality of drinking water as a result of industrial discharge and other man-made activities, posing a threat to human life. The slow self-deterioration of organic pollutants due to their stable structure is the most important issue. According to a World Health Organization (WHO) report, 785 million people lack access to basic drinking water, and half of the world's population will be living in water-scarce areas by 2025 [1].

Synthetic dyes, which are used to color plastic, paper, and artificial and natural fabrics, are water-soluble organic pollutants [2]. The usage of dye-tainted water poses a number of health hazards and can injure human organs [3]. Excessive discharge of organic dyes into the water environment prevents sunlight seepage, disrupting photochemical and biological activity of aquatic flora and fauna. They have been found to be very carcinogenic and poisonous [4–6].

Pharmaceuticals in water degrade the quality of drinking water supplies, contribute to antibiotic resistance, and are toxic to aquatic organisms. Pharmaceuticals have been placed on the European Union's and the US Environmental Protection Agency's water quality watch lists [7]. Tetracycline hydrochloride (TCH) release into the aquatic environment is seen as a concern to humans since it increases antibiotic resistance in some pathogenic bacteria and persists in the environment due to its non-biodegradability.

Surface water is polluted with many infectious microorganisms, such as bacteria (*E. coli*, *Vibrio*), viruses (such as Norwalk virus and rotavirus) and protozoans (such as *Entamoeba*,

*Giardia*) that are capable of causing illnesses in humans, such as bloody diarrhea, affecting human health as well as the environment. Because of their resistance to disinfection, they are the most commonly identified cause of waterborne illness.

Pesticides are another major organic pollutant in water bodies. The agriculture sector is the main source of pesticides into the aquatic environment, as they are used for destroying and controlling pests to protect crops. Their variety, toxicity, persistence and low biodegradability cause threat to humans through pollution of drinking water resources [8].

For the removal of organic contaminants, dyes, and pharmaceuticals from wastewater, a variety of technologies have been developed, including adsorption [9], chemical oxidation [10], advanced oxidation processes (AOPs), and biodegradation. Among them, AOPs have gained much attention because they are eco-friendly and economical. These processes include oxidation, photocatalysis, and electrochemical processes [11]. Photocatalysis is a very economical and extensively used AOP [12]. It requires UV or visible radiation for activation, but does not require massive machinery [13]. Due to its unique potential in deteriorating organic pollutants, it is widely used for wastewater treatment [14]. Due to its numerous favorable qualities, TiO<sub>2</sub> emerged as one of the most appropriate materials for environmental protection after the investigation of the Honda–Fujishima effect [15]. TiO<sub>2</sub> is non-toxic, and the US Food and Drug Administration has approved it for use in pharmaceuticals, human food, food-contact products, and cosmetics. The size of TiO<sub>2</sub> nanoparticles reduces as their surface area increases at the nanoscale level, which is one of the required properties of nanoparticles for photocatalytic applications [16–18]. When compared to other photocatalysts, TiO<sub>2</sub> is widely used for a variety of applications due to its optical, thermal/chemical stability, abundance, high redox potential, and electrical properties [19,20]. TiO<sub>2</sub> can absorb UV light due to a large bandgap (3.2 eV). Solar light has about 50% visible light and 5% UV light. Due to its band potential, TiO<sub>2</sub> can efficiently produce reactive oxygen species (ROS) in both oxidative and reductive pathways. There is need for photocatalysts to harvest solar energy for environmental remediation.

Ferrites, which are mixed metal oxides with iron as their major constituent, have emerged as one of the most intensely studied photocatalysts in the last decade due to their remarkable magnetic properties, small bandgap, superparamagnetic, tunable morphologies, high saturation field, non-toxicity, reusability, and chemical stability. Due to their small bandgaps (1.1–2.3 eV), ferrites absorb visible light. They are the most effective photocatalysts because they respond to the visible light spectrum correctly and can trap solar light for pollutant destruction. They have photocatalytic capabilities that are useful in a variety of industrial processes, such as exhaust gas treatment, alcohol and hydrogen peroxide decomposition, oxidative dehydrogenation of hydrocarbons, hydroxylation of phenol, and oxidation of CO, H<sub>2</sub>, CH<sub>4</sub> and chlorobenzene [21–23]. Ferrites' catalytic properties are increased by their magnetic nature and the ease with which they may be recovered using a magnet once the reaction is complete. Iron oxide particles have a high superparamagnetic and surface area-to-volume ratio due to their nanoscale size [24,25]. The vast surface-active sites and great adsorption capacity of iron oxide nanoparticles are because of their large surface area. Iron oxide nanoparticles in their pure, doped, and nanocomposite forms are widely used for environmental protection.

Magnetic nanoparticles have a number of disadvantages due to their aggregation-induced instability, which reduces their surface energy and makes them easier to oxidize in air. When magnetic nanoparticles clump together, they lose their magnetic properties and become dispersible. New ways for chemically stabilizing pure magnetic NPs are needed. Most studies show that coating magnetic NPs with silica (SiO<sub>2</sub>) prevents deterioration, oxidation of the magnetic core, and aggregation. Silica promotes effective transfer of photoinduced charge carriers, and its porous structure enhances the adsorption capacity and surface area of the system, thus increasing photocatalytic activity.

Because of outstanding physical, mechanical, and chemical properties, carbon nanomaterials such as fullerenes, carbon black, carbon nanotubes, diamond, graphene and carbon quantum dots have gained worldwide attention in the scientific community. Recently,

carbon quantum dots (CQDs) with size less than 10 nm have extensive applications in photovoltaic devices, fluorescent probes and bioimaging because of their excellent intrinsic low toxicity, excellent sunlight-harvesting ability, optical properties, eco-friendliness and chemical stability. Hybridization of carbon in CQDs is due to  $sp^3$ . Because of their conjugated structure, CQDs are good electron acceptors and transporters, and they have up-conversion photoluminescence (PL) characteristics. Functional groups on the surface can be changed depending on synthesis methods to fine-tune the PL of CQDs. CQDs have the ability to alter semiconductors in order to boost photocatalytic activity [26–29]. As a result, their industrial production and applications in such fields as research, environment, and medicine increased. Because of their low toxicity, high biocompatibility, stability, and ease of use, carbon quantum dots and silica are becoming more popular as coating materials.

Due to the smallness of non-magnetic photocatalysts such as semiconductors ( $TiO_2$ ,  $SiO_2$ , and CQDs) their separation and recovery after treatment is difficult, expensive, and time-consuming, and as a result, practical applications of non-magnetic photocatalytic semiconductors have decreased [30,31]. Adding spinel ferrite nanoparticles (SFNPs) to non-magnetic photocatalysts improves the ease of recovering photocatalysts from reaction mixtures after they have been employed, as well as the rate of pollutant degradation.

The assembly of nanoparticles of different materials in core–shell nanostructures has become increasingly attractive in recent years. Such nanoplatforms aim to integrate the specific characteristics of each material into a single, multifunctional entity capable of delivering a wide range of features. Potential applications of core–shell nanocomposites comprise heterogeneous catalysis, water remediation, optoelectronics and biomedical applications [32,33]. They have excellent magnetic separation properties, stability and good biocompatibility. They exhibit distinct qualities, such as a high surface area-to-volume ratio, a significant number of reactive sites available to enable the dispersal of organic pollutants on the surface and pores, tiny dimension, and high recovery capacity.  $Ag_2MoO_4/BiOBr$  heterojunction was used for the removal of organic pollutants [34]. Ghamkhari et al. and Mohammadi et al. synthesized a poly(styrene-block-acrylic acid) diblock copolymer-modified  $Fe_3O_4$  magnetite nanocomposite for removal of penicillin G and ciprofloxacin [35,36]. Neodymium oxide ( $Nd_2O_3$ ) nanoparticles and  $BaFe_{12}O_{19}/CoFe_2O_4$ @polyethylene glycol nanocomposites were used for the removal of acid dye [37,38]. Mohafez et al. and Davarpanah et al. used  $MnCe_{1.4}Fe_{0.6}O_4$  and  $BaFe_{12}O_{19}/CoFe_2O_4$  nanocomposites for removal of fungal and bacterial pathogens, respectively [39,40].

Several reviews and chapters have been published on the photocatalytic applications of spinel ferrite nanoparticles and nanocomposites in wastewater treatment, photocatalytic activity of CQDs [41] and on photocatalytic performance of  $TiO_2$  [42]. Ghasemi wrote a book on magnetic ferrite and related nanocomposites [43]. However, the research on nanocomposites of ferrites with  $TiO_2$ ,  $SiO_2$ , and CQDs as photocatalysts for degradation of organic pollutants and microbes has not been compiled as review till now. These three materials are commonly used for making nanocomposites of ferrites due to their ease of synthesis and low cost. The present review envisages the synthesis and structural features of nanocomposites of ferrites with  $TiO_2$ ,  $SiO_2$ , and CQDs. Their photocatalytic activity for degradation of organic pollutants and microbes is also elaborated upon.

## 2. Synthesis and Structural Features of Ferrite-Based Nanocomposites

To control size and surface area of materials, methods used to synthesize materials play an important role. Nanocomposites are multiphase solid materials with nanoscale repeat distances between phases and one, two, or three dimensions of less than 100 nm in one of the phases. The successful production of nanocomposites is indicated by homogeneous dispersion of nanometer-sized particles composing the dispersed phase in the matrix. Methods of synthesis of nanocomposites of ferrites with  $TiO_2$ ,  $SiO_2$ , and CQDs are given in Figure 1.

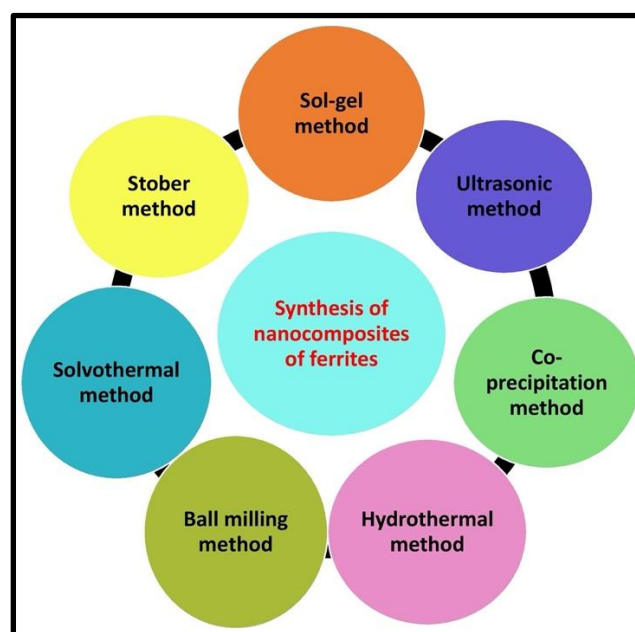


**Figure 1.** Methods of synthesis of NCs of ferrites with  $\text{TiO}_2$ ,  $\text{SiO}_2$ , and CQDs.

### 2.1. Magnetic Features of Ferrite Nanoparticles

Ferrite nanoparticles have chemical and physical characteristics that differ significantly from bulk ingredients, which can be related to their size. Every discrete magnetic nanoparticle behaves like a huge paramagnetic atom at the nanoscale, with a fast response to applied magnetic fields and apparent unique magnetic characteristics. Remnant magnetization ( $M_r$ ), saturation magnetization ( $M_s$ ), coercivity ( $H_c$ ), and magnetic anisotropy are the most essential magnetic characteristics of nanoparticles. Magnetic nanoparticles achieve a perfect magnetic moment in the presence of an external magnetic field (MF) due to parallel orientation of unpaired electrons, which is referred to as  $M_s$ . “ $M_r$ ” refers to the overall residual magnetization of the material after the removal of the MF due to a few unpaired electron orientations. The resistance of a ferromagnetic material towards becoming demagnetized is known as  $H_c$ , and it is used to categorize magnetic materials as hard or soft. “Magnetocrystalline anisotropy” (MCA) is another important term used to characterize the magnetic property of nanoparticles, and it represents the orientations of the magnetic moments at a given time in the direction of their ideal easy axes. Spin–orbit interaction is the principal source of MCA, especially in isolated systems, and is responsible for keeping the spins in a certain orientation. It has a direct impact on magnetic characteristics such as  $M_r$ ,  $M_s$ , and  $H_c$ . Cation distribution on the octahedral and tetrahedral sites, as well as the size and shape of the nanoparticles, usually regulate these magnetic characteristics. In fact, the total magnetic moment of spinel ferrite nanoparticles is primarily determined by the difference in the exchange interaction of valence electrons of cations located at A and B sites. This is because the magnet’s electron spin is well-organized and parallel inside each lattice site, but antiparallel between the two sublattice sites. However, the contribution of the A-A and B-B interactions is negligible.

### 2.2. Nanocomposites of Ferrites with $\text{TiO}_2$

$\text{TiO}_2$  has four polymorphs: brookite (orthorhombic), rutile (tetragonal), anatase (tetragonal) and  $\text{TiO}_2$ -B, as shown in Figure 2. Anatase, rutile, and brookite phases have bandgaps of 3.2, 3.0, and 3.4 eV, respectively. Brookite is less thermodynamically stable, but rutile is stable and anatase is metastable. At temperatures exceeding 600 °C, irreversible conversion of brookite and anatase  $\text{TiO}_2$  to rutile occurs [44].

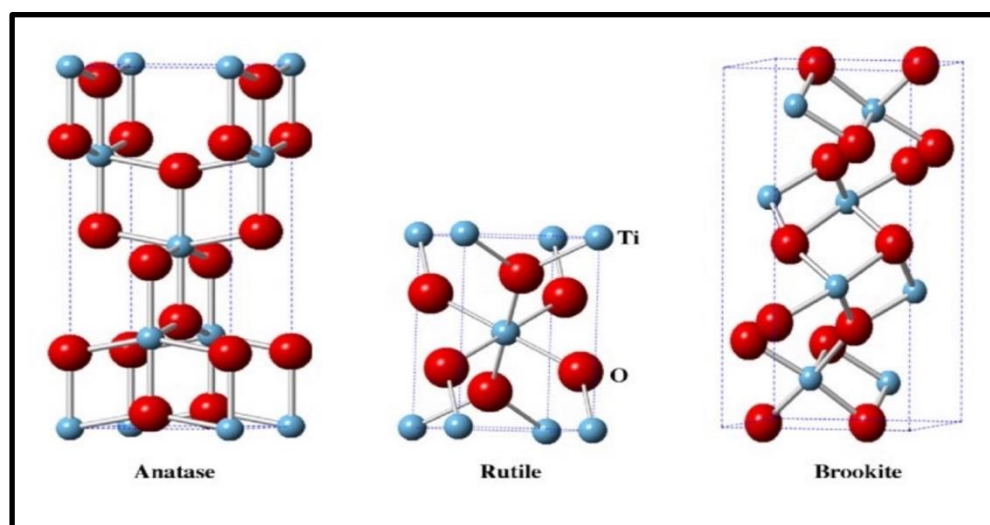


**Figure 2.** Three polymorphs of  $\text{TiO}_2$  (adapted from with the permission from Ref. [44], 2020, *Chemical Engineering Journal*).

It has been observed that bandgaps of  $\text{TiO}_2$  nanoparticles with 5–10 nm particles narrow up to 0.2 eV. Anatase is the most photocatalytically effective phase of  $\text{TiO}_2$  [45] and is widely used in semiconducting materials for environmental applications [46]. It has higher mobility of electron–hole pairs and higher surface hydroxyl density. Brookite-phase activity has not been thoroughly examined [47,48]. Rutile  $\text{TiO}_2$  is usually investigated in fundamental investigations. Due to the existence of oxygen vacancies,  $\text{TiO}_2$  is classed as an n-type semiconductor [49]. Because crystalline  $\text{TiO}_2$  has a less photoexcited electron–hole recombination than amorphous  $\text{TiO}_2$ , it has higher photocatalytic activity [50,51]. Recombination of photogenerated charge carriers is a disadvantage of  $\text{TiO}_2$  photocatalysts, as it decreases overall reaction quantum efficiency [52]. During the recombination processes, the photoexcited electrons return to the valence band non-radiatively or radiatively [53–55]. An attractive feature of the  $\text{TiO}_2$  photocatalyst is its potential to be activated by visible light. To increase photocatalytic activity and decrease recombination of photoexcited charge carriers, several methods have been followed, such as heterojunction formation and doping with non-metals, metals, and nanosized crystals, which can alter the electronic and optical properties of  $\text{TiO}_2$  [56–60]. By using dopants in  $\text{TiO}_2$ , its bandgap reduces [61]. Metal doping has long been known to improve visible light absorbance of  $\text{TiO}_2$  [62,63] and increase its photocatalytic activity under UV irradiation [63–66], but the introduction of metal ion results in thermal instability, which reduces the reuse of  $\text{TiO}_2$  photocatalyst and recombination of electron–hole pairs occur at a fast rate. Non-metal doping is more efficient than metal ion doping due to more thermal stability and less formation of recombination centers [67–71].

Nanocomposites of ferrites with  $\text{TiO}_2$  have been synthesized using different chemical methods. A summary of methods used to synthesize magnetic nanocomposites has been discussed in this section.

### 2.2.1. Sol–Gel Method

In typical sol–gel synthesis, formation of gel materials with three-dimensional structure occurs by condensation and hydrolysis reaction of metal ions. It is an irreversible process: once gel is formed, it cannot break down. There is covalent interaction between gel particles. In this method, huge precursors are used during conversions and can be performed at or near room temperature. For chemical catalysts, porous ceramic xerogels with large surface area act as support and thin-film deposition is important for material possessing desired optical and magnetic properties [24]. This method uses simple equipment, produces highly

homogeneous and pure products at low temperatures, and allows modification of the surface.

Tatarchuk et al. [72] developed magnetic nanocomposites of  $\text{CoFe}_2\text{O}_4@\text{TiO}_2$  using the Pechini sol–gel method with ethylene glycol and citric acid as chelating agents and titanium (IV) polymeric precursor solution. XRD study of  $\text{CoFe}_2\text{O}_4@\text{TiO}_2$  indicated the presence of 46% and 54% of anatase and rutile crystal phase, respectively, in the titanium dioxide ( $\text{TiO}_2$ ) component, and the average size of cobalt ferrite ( $\text{CoFe}_2\text{O}_4$ ) and  $\text{TiO}_2$  nanoparticles was about 30 and 8 nm, respectively. SEM revealed that because of deposition of  $\text{TiO}_2$  on the  $\text{CoFe}_2\text{O}_4$  surface, particles became large. The IR spectrum of the nanocomposite illustrated the shift of bands, which was the result of isomorphous heterovalent substitution in the octahedral position. Dadfar et al. [73] and Xu et al. [74] fabricated  $\text{SrFe}_{12}\text{O}_{19}/\text{TiO}_2$  and  $\text{TiO}_2/\text{ZnFe}_2\text{O}_4$  nanostructures by the sol–gel method. XRD indicated the presence of impurity phases ( $\alpha\text{-Fe}_2\text{O}_3$ ) at pH 2.5 and 4.5, while pure  $\text{SrFe}_{12}\text{O}_{19}$  and  $\text{TiO}_2$  phases were formed at pH 3.5. The production of the rutile phase was prohibited to some extent by highly dispersed  $\text{ZnFe}_2\text{O}_4$  nanoparticles in  $\text{TiO}_2/\text{ZnFe}_2\text{O}_4$  nanocomposites. TEM confirmed average particle sizes of 15–75 nm of  $\text{SrFe}_{12}\text{O}_{19}/\text{TiO}_2$  and uniform attachment of  $\text{ZnFe}_2\text{O}_4$  nanoparticles to  $\text{TiO}_2$  nanoparticles to produce a coupled semiconductor. The electron diffraction pattern displayed very weak intensity of the electron diffraction pattern for the  $\text{ZnFe}_2\text{O}_4$  phase, which was attributed to the dispersion of  $\text{ZnFe}_2\text{O}_4$  nanoparticles amid the  $\text{TiO}_2$  nanoparticles. The value of saturation magnetization, remnant magnetization, and coercivity decreased with increasing amounts of  $\text{TiO}_2$  in  $\text{TiO}_2/\text{ZnFe}_2\text{O}_4$ , due to the contribution of the non-magnetic  $\text{TiO}_2$  component to total sample volume.

Lahijani et al. [75] fabricated a  $\text{PbFe}_{12}\text{O}_{19}\text{-TiO}_2$  nanocomposite using the sol–gel method. From XRD analysis, the average size of crystals was found to be 88 nm. FTIR study indicated that absorption bands at 544, 716, 935 and  $1401\text{ cm}^{-1}$  corresponded to stretching modes of Fe–O, Ti–O, Pb–O and C–C bonds, respectively. Heating the compound in the presence of a polyhydroxy alcohol, such as ethylene glycol, promotes polymerization. The metal ions are equally dispersed inside the organic matrix, resulting in a homogeneous resin—the polymeric precursor [76]. The immobilization of metal complexes in such rigid organic polymeric networks can decrease segregation of specific metals, ensuring molecular compositional uniformity. Polymeric precursors can be used to make ferrite– $\text{TiO}_2$  nanocomposites. Mouro et al. [77] used a polymeric precursor technique to make nanometric  $\text{TiO}_2/\text{CoFe}_2\text{O}_4$  composites. X-ray diffraction, Raman spectroscopy, surface area through  $\text{N}_2$  physisorption, zeta potential, scanning and high-resolution transmission electron microscopy were used to characterize the as-prepared sample. The lack of a rutile phase in the nanocomposites was confirmed by Raman spectroscopy. XRD patterns revealed that thermal treatment did not cause phase segregation. The synthesized nanocomposites showed an increase in surface area, a change in surface charge in relation to pure  $\text{TiO}_2$ , and selectivity in the photodegradation. The materials had photocatalytic activity due to the presence of  $\text{TiO}_2$  on their surfaces, and  $\text{CoFe}_2\text{O}_4$  cores were beneficial for separating and recovering photocatalysts after use in an oxidative process.

### 2.2.2. Ultrasonic Method

The ultrasonic technique involves using sound energy to agitate the particles in a solution, resulting in physical and chemical changes. This method is found to be the most promising method for manufacturing nanocomposites such as oxides, carbides, alloys and colloids with almost uniform distribution of nanoparticles [78]. Ultrasound irradiation causes unstable bubbles in liquids to form, grow, and collapse rapidly at temperatures as high as 5000 K, pressures as high as 20 MPa, and cooling speeds of  $10^{10}\text{ Ks}^{-1}$  [79]. Ultrasonication was used for the synthesis of titania-coated  $\gamma\text{-Fe}_2\text{O}_3$  magnetic activated carbon and  $\text{Fe}_3\text{O}_4\text{-TiO}_2$  photocatalyst with saturation magnetization value of 2.21 and  $14\text{ emug}^{-1}$ , respectively [80,81]. XRD revealed that the titania coated on the magnetic activated carbon maintained the anatase phase, with the same set of characterization peaks for both  $\text{Fe}_3\text{O}_4$  and  $\text{Fe}_3\text{O}_4\text{-TiO}_2$ , indicating that the ultrasound irradiation had no effect on

the crystal structure of the  $\text{Fe}_3\text{O}_4$  nanoparticles. The tiny crystallite size was shown by the broad nature peak of the deposited  $\text{TiO}_2$  on  $\text{Fe}_3\text{O}_4$ - $\text{TiO}_2$ . SEM revealed the homogeneous distribution of titania. Superparamagnetic characteristics of  $\text{Fe}_3\text{O}_4$ - $\text{TiO}_2$  photocatalyst at room temperature were confirmed by a magnetization hysteresis loop. HRTEM analysis showed the occurrence of a heterojunction in the  $\text{Fe}_3\text{O}_4$ - $\text{TiO}_2$  nanocomposite. XPS showed that the peaks at 710.5 eV and 458.8 eV originated from Fe 2p and Ti 2p energy levels, respectively, implying that  $\text{Fe}_3\text{O}_4$  and  $\text{TiO}_2$  were largely present as separated phases in  $\text{Fe}_3\text{O}_4$ - $\text{TiO}_2$  composites.

### 2.2.3. Coprecipitation Method

This approach requires the preparation of a mixed aqueous solution of starting chemicals such as chlorides, nitrates, or sulfites of  $\text{Fe}^{3+}$ , as well as of divalent metal ions in the requisite stoichiometric ratio. The precipitates are then generated by treating the solution with NaOH, filtration, washing twice, and drying. This approach entails four steps: nucleation, growth, coarsening, and agglomeration, all occurring at the same time [82]. Nanocomposites of ferrites of good quality and phase purity can be obtained by this method. This process offers various advantages such as high yield, high product purity, lack of necessity to use organic solvent, good reproducibility and low cost. It is a quick and easy way to make ultrafine particles that are disseminated in a variety of media. By carefully monitoring the preparation parameters, it is possible to achieve control over the surface morphology, structure, and chemical composition with this procedure.

Coprecipitation was employed for fabrication of  $\text{CoFe}_2\text{O}_4/\text{TiO}_2$  and  $\text{ZnFe}_2\text{O}_4$ - $\text{TiO}_2$  nanocatalysts [83,84]. The average particle size of the coprecipitated nanocatalysts was 50 nm for  $\text{CoFe}_2\text{O}_4$  and 150 nm for  $\text{CoFe}_2\text{O}_4/\text{TiO}_2$  according to SEM images, which was consistent with the crystallite size predicted from XRD data. The spherical geometry ( $9 \pm 2$  nm) of  $\text{ZnFe}_2\text{O}_4$  nanoparticles and spherical-like morphology ( $11 \pm 3$  nm) of  $\text{ZnFe}_2\text{O}_4$ - $\text{TiO}_2$  nanocomposites and fine dispersion of black particles ( $\text{CoFe}_2\text{O}_4$ ) on the gray surface ( $\text{TiO}_2$ ) of  $\text{CoFe}_2\text{O}_4/\text{TiO}_2$  were depicted in the TEM images (Figure 3). Bandgaps of  $\text{CoFe}_2\text{O}_4/\text{TiO}_2$ ,  $\text{CoFe}_2\text{O}_4$ ,  $\text{ZnFe}_2\text{O}_4$ - $\text{TiO}_2$ , and  $\text{ZnFe}_2\text{O}_4$  were found to be 2.8, 1.1, 2.3, and 2.1 eV, respectively, which suggested the formation of a visible light-active photocatalyst. The large bandgap of the composite may be due to the mixing effect of the bandgap and the interfacial coupling effect between  $\text{ZnFe}_2\text{O}_4$  and  $\text{TiO}_2$ ,  $\text{CoFe}_2\text{O}_4$  and  $\text{TiO}_2$ . XRD pattern analysis revealed that in  $\text{CoFe}_2\text{O}_4/\text{TiO}_2$ , the conversion of anatase to the rutile phase of  $\text{TiO}_2$  happened at a  $\text{TiO}_2$  annealing temperature of  $\leq 600$  °C, confirming the purity of  $\text{ZnFe}_2\text{O}_4$  and  $\text{TiO}_2$  phase in  $\text{ZnFe}_2\text{O}_4$ - $\text{TiO}_2$ , which was in agreement with HRTEM and SAED investigations. Haw et al. [85] found that in comparison to conventional rutile-phase  $\text{TiO}_2$  and pure urchin-like  $\text{TiO}_2$  (3D  $\text{TiO}_2$ ) microparticles, nanocomposites of  $\text{CoFe}_2\text{O}_4$ -3D  $\text{TiO}_2$  showed an increase in photodegradation of methylene blue, and this nanocomposite demonstrated a generally constant photocatalytic efficacy with low degradation. Two sets of lattice fringes were visible at the  $\text{TiO}_2$ - $\text{CoFe}_2\text{O}_4$  interface, with  $d_{110} = 0.322$  nm of rutile phase titania and  $d_{331} = 0.193$  nm of  $\text{CoFe}_2\text{O}_4$ . The  $\text{CoFe}_2\text{O}_4$  nanoparticles were clearly visible on the 3D urchin-like  $\text{TiO}_2$  structure, and each element was uniformly distributed over the surface of the  $\text{TiO}_2$  microsphere on scanning transmission electron microscopy. XRD peaks were designated to the rutile phase of 3D urchin-like  $\text{TiO}_2$  and broader peaks confirmed the presence of nanosized  $\text{CoFe}_2\text{O}_4$  in the sample.

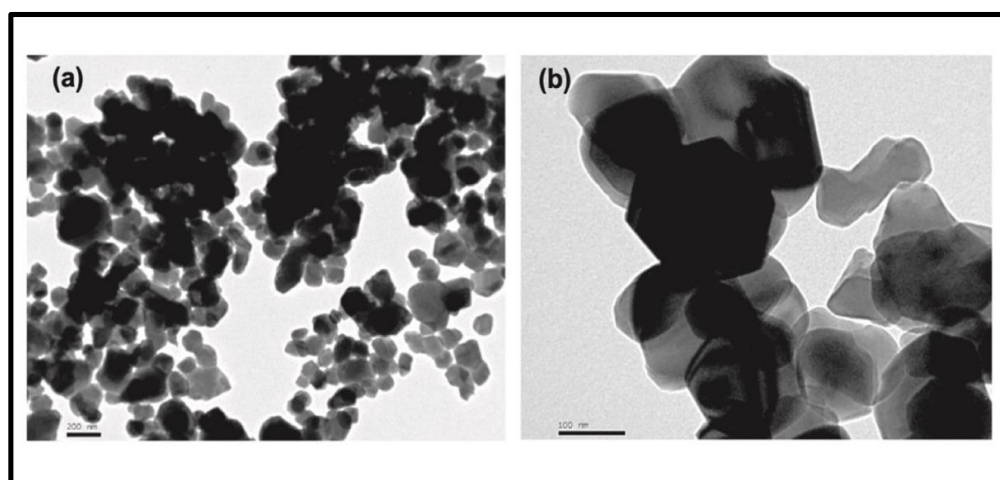


**Figure 3.** TEM photographs of  $\text{CoFe}_2\text{O}_4/\text{TiO}_2$  nanocatalysts confirms the fine dispersion of black particles ( $\text{CoFe}_2\text{O}_4$ ) on the gray surface ( $\text{TiO}_2$ ) at (a) 200 nm and (b) 100 nm (adapted from with the permission from Ref. [83], 2013, *Chemical Engineering Journal*).

#### 2.2.4. Hydrothermal Method

The hydrothermal method is a way of crystallizing a chemical, utilizing an aqueous solution at a high vapor pressure as well as temperature [86]. At standard temperatures ( $100\text{ }^\circ\text{C}$ ) and pressures ( $<1\text{ atm}$ ), it is generally depicted as crystal formation or crystal synthesis from insoluble chemicals. Autoclaves are used to carry out the process, which is performed at a controlled pressure and temperature. This enables the utilization of temperatures that are higher than the boiling point of water or an organic solution. The concoction reaction that occurs beyond the dissolvable breaking point and at pressures over bar is known as hydrothermal synthesis. The hydrothermal technique has the following advantages: it is simple to acquire nanotube morphology, variations in the synthesis process may be used to improve  $\text{TiO}_2$  nanotube characteristics, and it is a method that can be used for a variety of applications.

Hydrothermal deposition of a hard ferromagnetic strontium ferrite ( $\text{SrFe}_{12}\text{O}_{19}$ ) over  $\text{TiO}_2$  can result in a photocatalyst that is both ferromagnetic and visible light-active. The  $\text{TiO}_2$ -supported  $\text{SrFe}_{12}\text{O}_{19}$  nanocomposite has a strong ferromagnetic property and is quite stable when it comes to losing its magnetic property. XRD images of  $\text{TiO}_2$ -supported  $\text{SrFe}_{12}\text{O}_{19}$  nanocomposite correspond to mixture of anatase and rutile crystal phases. EDS results confirmed that  $\text{TiO}_2$ -supported  $\text{SrFe}_{12}\text{O}_{19}$  consists of Fe, Ti, Sr, C, O and Si. The BET-specific surface area of  $\text{TiO}_2$  was  $49.5\text{ m}^2\text{g}^{-1}$  with a total pore volume of  $0.1553\text{ cm}^3\text{g}^{-1}$ , which compares with  $38.3\text{ m}^2\text{g}^{-1}$  and  $0.0155\text{ cm}^3\text{g}^{-1}$  for  $\text{TiO}_2$ -supported  $\text{SrFe}_{12}\text{O}_{19}$ . Due to the deposition of  $\text{SrFe}_{12}\text{O}_{19}$  nanoparticles onto the  $\text{TiO}_2$ , the surface area and pore volume of the  $\text{TiO}_2$  nanocomposite reduces. The paramagnetic impact of  $\text{TiO}_2$  lowered the coercivity ( $H_C$ ) and saturation magnetization ( $M_S$ ) of  $\text{TiO}_2$ -supported  $\text{SrFe}_{12}\text{O}_{19}$ . The photocatalyst  $\text{TiO}_2$ -supported  $\text{SrFe}_{12}\text{O}_{19}$  had  $H_C$  of 2125.5 G. The coercivity of  $\text{TiO}_2$ -supported  $\text{SrFe}_{12}\text{O}_{19}$  nanocomposite showed that it was a good ferromagnetic material [87]. Nguyen and Doong [88] and Pongwan et al. [89] fabricated  $\text{ZnFe}_2\text{O}_4\text{-TiO}_2$  and  $\text{CoFe}_2\text{O}_4/\text{TiO}_2$  nanostructure photocatalysts by the hydrothermal method. The  $\text{ZnFe}_2\text{O}_4\text{-TiO}_2$  nanocomposite was prepared by coupling 0.2–2 wt % narrow-bandgap material of p-type  $\text{ZnFe}_2\text{O}_4$  with n-type anatase  $\text{TiO}_2$ . Transmission electron microscopy (TEM) and high-resolution TEM confirmed average particle sizes of 8–9 nm and 5–35 nm for  $\text{ZnFe}_2\text{O}_4\text{-TiO}_2$  and  $\text{CoFe}_2\text{O}_4/\text{TiO}_2$ , respectively. It was observed that  $\text{ZnFe}_2\text{O}_4$  and  $\text{TiO}_2$  were intimately linked, which led to a decrease in electron–hole recombination rate as well as enhanced photocatalytic activity of  $\text{ZnFe}_2\text{O}_4\text{-TiO}_2$  heterostructures under visible light irradiation. When the loading amount of  $\text{ZnFe}_2\text{O}_4$  increased from 0.5 to 2 wt %, SEM revealed a slight increase in particle size of  $\text{ZnFe}_2\text{O}_4\text{-TiO}_2$  nanocomposites. The  $\text{N}_2$  adsorption–desorption isotherms showed that the combination of  $\text{TiO}_2$  with  $\text{ZnFe}_2\text{O}_4$  can increase the specific

surface area. XRD analysis indicated that  $\text{ZnFe}_2\text{O}_4\text{-TiO}_2$  can retain the crystallinity of both nanoparticles. Electron diffraction pattern of  $\text{CoFe}_2\text{O}_4/\text{TiO}_2$  displayed the brightness of polymorphic discrete rings of the crystalline particles, suggesting quite a high degree of crystallinity in polycrystals. In this study, the obtained maximum saturation magnetization and coercivity of  $\text{CoFe}_2\text{O}_4$  and  $\text{CoFe}_2\text{O}_4/\text{TiO}_2$  nanocomposites were found to be 32.58, 29.64  $\text{emu g}^{-1}$  and 0.15, 0.05 kOe, respectively.

#### 2.2.5. Solvothermal Method

The solvothermal technique employs a non-aqueous solvent and a considerably higher temperature, allowing high boiling point solvents to be utilized. The solvothermal method outperforms the hydrothermal method in terms of shape, size control, distribution, and crystallinity of nanoparticles [90]. Organic solvents, which have a low relative permittivity and are free of ionic species, are used in the solvothermal process to produce a product devoid of foreign anions and ionic species. The benefits of both the hydrothermal and sol-gel methods are combined in this technique. This approach may be utilized in the ceramics sector to regulate the particle size of synthesized materials and to fabricate tiny particles, such as magnetic titania photocatalyst [91]. Atacan et al. [92] developed  $\text{ZnFe}_2\text{O}_4/\text{Ag-TiO}_2$  by the solvothermal method. The formation, structure and morphology of prepared samples were characterized by X-ray diffraction, scanning electron microscopy, Fourier-transform infrared spectroscopy and vibrating sample magnetometry. In this study, the obtained value of saturation magnetization of  $\text{ZnFe}_2\text{O}_4/\text{Ag-TiO}_2$  was 5.5  $\text{emu g}^{-1}$ . XRD patterns indicated that no chemical reaction occurred between  $\text{ZnFe}_2\text{O}_4$  and  $\text{Ag-TiO}_2$ , because no peaks related to other impurities were observed. Nguyen and Doong [93] synthesized  $\text{ZnFe}_2\text{O}_4/\text{TiO}_2$  heterostructure by this method.

### 2.3. Nanocomposites of Ferrites with Silica

Because of the Van der Waals forces of attraction between magnetic particles and their large surface area, they clump together, making it difficult to determine their physicochemical characteristics. One of the excellent methods to reduce particle agglomeration and to stabilize magnetic nanoparticles is the dispersion of magnetic nanoparticles in a silica matrix. Due to biocompatibility and chemical inertness, silica does not affect the redox reaction at core surface and assists the functioning of nanocomposites in a biological environment. This sort of matrix can help to reduce toxicity, increase biocompatibility, and shield encapsulated components from harsh reaction media. The properties of such nanocomposites might provide a number of advantages, including improved catalytic, magnetic, and mechanical capabilities [94,95]. Thus, silica-coated magnetic nanoparticles are becoming a promising and important approach in the development of magnetic nanoparticles for both fundamental studies and technological applications. Therefore, coating magnetic particles with silica allows its surface to conjugate with various functional groups. The optical properties of nanoparticles can also be increased by coating of silica gel [96]. Nanocomposites consisting of nanoscale magnetic particles embedded in an insulating matrix such as silica presented considerable difference in magnetic properties when compared with their equivalent pure and bulk materials. In this section, techniques for synthesis of ferrite-silica nanocomposites are discussed.

#### 2.3.1. Sol-Gel Auto-Combustion Method

Exothermic chemical reactions occur in the sol-gel process, and self-ignition of the gel occurs as a result of the combustion of the gel, resulting in black-brown powder as a product. Urea, glycine, citric acid, hydrazine, and carbohydrazide are common starting materials for this process, and stoichiometry and crystallite size can be easily adjusted. Colloidal gel is created by combining metal nitrate and an organic solvent, then adding  $\text{NH}_4\text{OH}$  to alter the pH. Sol-gel auto-combustion was used to synthesize  $\text{CoFe}_2\text{O}_4\text{-SiO}_2$  nanostructures by using metal nitrates as precursors. Bardapurkar et al. [97] studied  $(\text{CoFe}_2\text{O}_4)_x(\text{SiO}_2)_{1-x}$  synthesis, structural, spectral, and magnetic characteristics, where  $x$  ranged from 0.1 to 1.0. The

crystal structure, cation distribution, and band locations of silica matrix were detected in IR spectra. Crystallite size and pore fraction were at their maximum when the sample had the highest silica concentration, due to changes in inter-particle distances and crystallite size following dispersion in the matrix. As the ferrite-silica ratio was increased, the saturation magnetization dropped from  $68.7 \text{ emug}^{-1}$  to  $4.77 \text{ emug}^{-1}$ , indicating that the magnetic characteristics may be changed by altering the ferrite-silica ratio. The reduction in magnetization for the coated sample may be attributed to the presence of a non-magnetic silica layer on the surface of magnetic nanoparticles that reduces the particle-particle interaction and lowers the exchange coupling energy, which in turn reduces the magnetization. In the FTIR spectra, there were strong absorption bands found around  $1090 \text{ cm}^{-1}$  and  $800 \text{ cm}^{-1}$  that corresponded to silica network.  $\text{SiO}_2$ -coated cobalt ferrite nanocomposites were fabricated by Gharagozlou [98] and Pansambal et al. [99] using tetrakis(2-hydroxyethyl) orthosilicate (THEOS) and tetraethyl orthosilicate (TEOS) as water-soluble silica precursors, respectively. TEM images revealed that spherical, non-agglomerated cobalt ferrite nanoparticles were homogeneously distributed in the silica matrix. Saturation magnetization was found to be less for nanocomposite compared to bare nanoparticles. Peaks present in the XPS spectra of  $\text{CoFe}_2\text{O}_4/\text{SiO}_2$  corresponded to Co 2p, Fe 3p, Fe 2p, Si 2s, Si 2p signals, which confirmed the formation of  $\text{CoFe}_2\text{O}_4/\text{SiO}_2$ . There was no unidentified peak in the EDX data, which confirmed the purity, elemental composition and formation of  $\text{CoFe}_2\text{O}_4/\text{SiO}_2$ . Specific surface area of  $\text{CoFe}_2\text{O}_4/\text{SiO}_2$  was  $9.34 \text{ m}^2\text{g}^{-1}$  calculated by BET equation. Results indicated that crystallization, saturation magnetization  $M_s$  and remanent magnetization  $M_r$  escalates as the calcination temperature rises, but the variation in coercivity  $H_c$  was not in accordance with that of  $M_s$  and  $M_r$ , indicating that  $H_c$  is not determined only by the crystallinity and size of  $\text{CoFe}_2\text{O}_4$  nanoparticles. Figure 4 shows a technological scheme for the synthesis of ferrite-silica nanocomposite. The influence of chelator chain length on precursor formation and decomposition to nanocomposites of ferrite with  $\text{SiO}_2$  was studied. Dippong et al. [100] prepared  $\text{CoFe}_2\text{O}_4/\text{SiO}_2$  nanocomposite by using three short-chain diols (1,2-ethanediol, 1,3-propanediol, and 1,4-butanediol) as chelators. The influence of the methylene groups' numbers in the precursors and annealing temperature on the nanocrystallite size was revealed. This method provides some advantages in making silica composite material containing highly dispersed nanoparticles and promotes a good and homogeneous dispersion of particles into silica matrix.

### 2.3.2. Stöber Method

A system of chemical reactions has been developed that allows the controlled growth of spherical silica particles of uniform size by means of hydrolysis of alkyl silicate and subsequent condensation of silicic acid in alcoholic solutions. The schematic procedure employed for the synthesis of  $\text{MgFe}_2\text{O}_4\text{-SiO}_2$ ,  $\text{Co}_{1-x}\text{Zn}_x\text{Fe}_2\text{O}_4/\text{SiO}_2$ ,  $\text{CoFe}_2\text{O}_4/\text{SiO}_2$  was reported [101]. Eromosele et al. [102] and Khanna and Verma [103] developed  $\text{SiO}_2$ -coated  $\text{MgFe}_2\text{O}_4$  and  $\text{KFeO}_2$  by Stöber method, respectively. Both bare and  $\text{SiO}_2$ -coated  $\text{KFeO}_2$  exhibited orthorhombic structure, whereas bare and silica-coated magnesium ferrite exhibited a single cubic spinel phase. Association of silica on the surface of  $\text{MgFe}_2\text{O}_4$  and  $\text{KFeO}_2$  nanoparticles was confirmed by EDAX in  $\text{MgFe}_2\text{O}_4\text{-SiO}_2$  and by FTIR in  $\text{KFeO}_2/\text{SiO}_2$ . It was further confirmed by FTIR data in  $\text{MgFe}_2\text{O}_4\text{-SiO}_2$ , because in coated samples, there was a shift in stretching vibration of Fe-O from  $560 \text{ cm}^{-1}$  to  $574 \text{ cm}^{-1}$  due to silica coating. It was observed that due to silica coating, the crystallite size reduced from 53 to 47 nm in  $\text{MgFe}_2\text{O}_4\text{-SiO}_2$ , but in  $\text{KFeO}_2/\text{SiO}_2$ , it increased from 4–8 nm to 10–22 nm. Values of saturation magnetization of  $\text{MgFe}_2\text{O}_4\text{-SiO}_2$  and  $\text{KFeO}_2/\text{SiO}_2$  were 22 and  $21.17 \text{ emug}^{-1}$  and possessed ferrimagnetic and superparamagnetic behavior, respectively, at room temperature. Figure 5 shows a schematic representation of  $\text{SiO}_2$  coating of  $\text{MgFe}_2\text{O}_4$ .

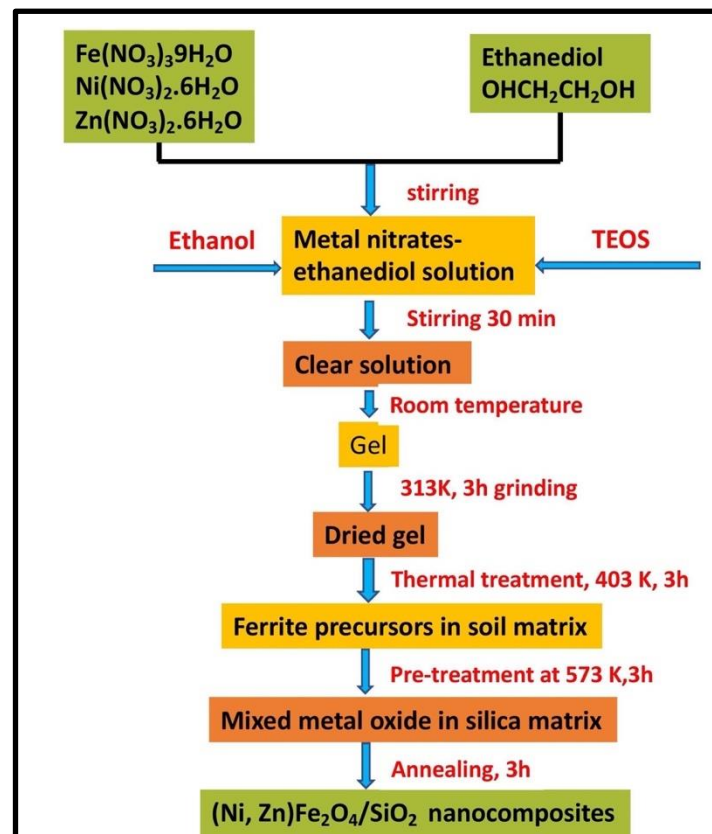


Figure 4. Scheme for the synthesis of ferrite–silica nanocomposite via sol–gel method.

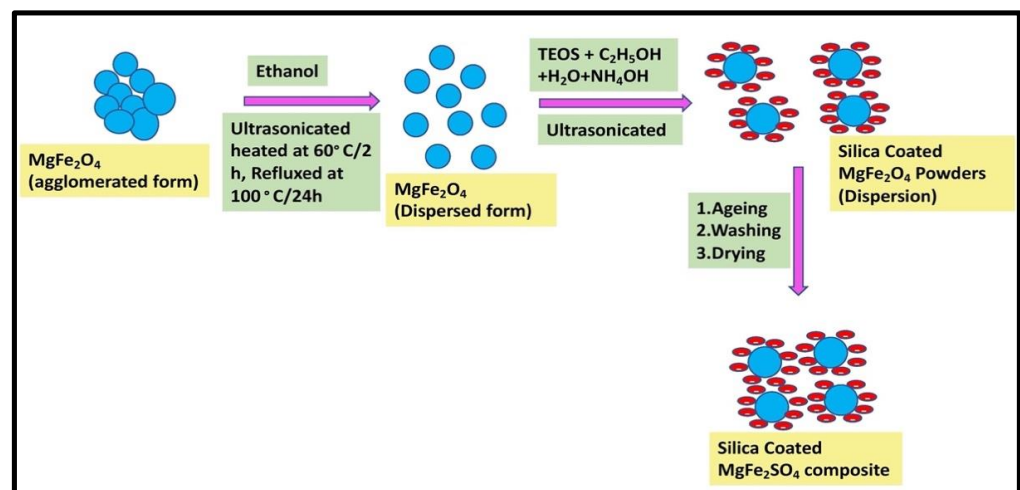


Figure 5. Schematic representation of silica coating of  $\text{MgFe}_2\text{O}_4$ .

The influence of aging temperature on the synthesis of nanocomposites of ferrites with silica by the Stöber method was studied. Queiroz et al. [104] investigated various aging temperatures—98, 80, 60, 27/98, and 27 °C—for the synthesis of silica-coated cobalt ferrite. Aging temperatures of 98 and 27/98 °C give the best suited conditions for preparing the single phase of cobalt ferrite. The presence of silica on the particle surface was confirmed using diffuse reflectance infrared Fourier transform, which presented vibrational modes with asymmetric stretching absorption in the region 900–1200  $\text{cm}^{-1}$  associated with the Si-OH and O-Si-O groups and value of saturation magnetization of coated samples of 10.05  $\text{emu g}^{-1}$ . Girgis et al. [105] studied the magnetic and optical properties of  $\text{CoFe}_2\text{O}_4$ ,

$\text{ZnFe}_2\text{O}_4$ ,  $\text{Co}_{0.5}\text{Zn}_{0.5}\text{Fe}_2\text{O}_4$  coated with silica by heating at 400, 600 and 800 °C. It was observed that by raising the temperature from 400 to 800 °C, average crystallite size of core-shell nanocomposites increase.

### 2.3.3. Coprecipitation Method

This method was used for the formation of nanocomposites of ferrites with silica using different precursors.  $\text{SiO}_2$ -coated cobalt ferrite nanocomposites were fabricated using metallic chlorides and metal nitrate as precursors and annealing at 100, 200, and 300 °C and 250, 500, and 750 °C, respectively. The coercivity and saturation magnetization of nanocomposite (annealed at 300 °C for 2 h) were much higher than that of bulk cobalt ferrite.  $\text{CoFe}_2\text{O}_4$  nanocrystallites were observed in the silica matrix during the annealing of samples, and their size increased with increasing annealing temperature. TEM showed that homogeneously distributed, well-crystallized, and nearly spherical  $\text{CoFe}_2\text{O}_4$  nanoparticles were inserted in the silica host matrix (Figure 6). FTIR spectra showed that as annealing temperature increased, the absorption peaks at  $1090\text{ cm}^{-1}$  for Si-O-Si further broadened [106]. The broad hump in the X-ray diffraction pattern at  $2\theta \sim 18^\circ\text{--}23^\circ$  corresponds to the presence of amorphous silica in the sample. An increase in crystallite size of  $\text{CoFe}_2\text{O}_4\text{:SiO}_2$  nanocomposites was observed from 20.26 to 28.95 nm and 38.76 nm with increase in calcination temperature from 250 to 500 °C and 750 °C by the Williamson–Hall method. Moreover, lattice parameter and strain values increased from 8.0321 to 8.0691 Å and  $1.01 \times 10^{-2}$  to  $3.75 \times 10^{-3}$ , respectively, as temperature increased from 250 to 750 °C. SEM analysis revealed the formation of well-developed nanoparticles of  $\text{CoFe}_2\text{O}_4\text{:SiO}_2$  with intergranular porosity [107]. Yakob et al. [108] prepared  $\text{CoFe}_2\text{O}_4\text{/SiO}_2$  by coprecipitation using metal nitrate as precursor. The polycrystalline and spinel crystal structure of  $\text{CoFe}_2\text{O}_4\text{/SiO}_2$  with Fd3m group space was determined using XRD analysis.  $\text{CoFe}_2\text{O}_4\text{/SiO}_2$  crystallite nanoparticles were  $29.4 \pm 0.2\text{ nm}$  in size, whereas  $\text{CoFe}_2\text{O}_4$  was  $26.8 \pm 0.2\text{ nm}$ . Sharma et al. [109] calcined a  $\text{NiFe}_2\text{O}_4\text{/SiO}_2$  composite at temperatures of 300 to 900 °C. It was discovered through Rietveld refining that the powdered combination contains two phases: silicon dioxide and nickel ferrite. As a result, the sample has a cubic phase with space group Fd-3 m (227), with Fe atom at 32e site (3/8, 3/8, 3/8), O (oxygen) atom at 32e site (0.387, 0.387 and 0.387) and Ni atom at Wyckoff 8a site (0, 0, 0).

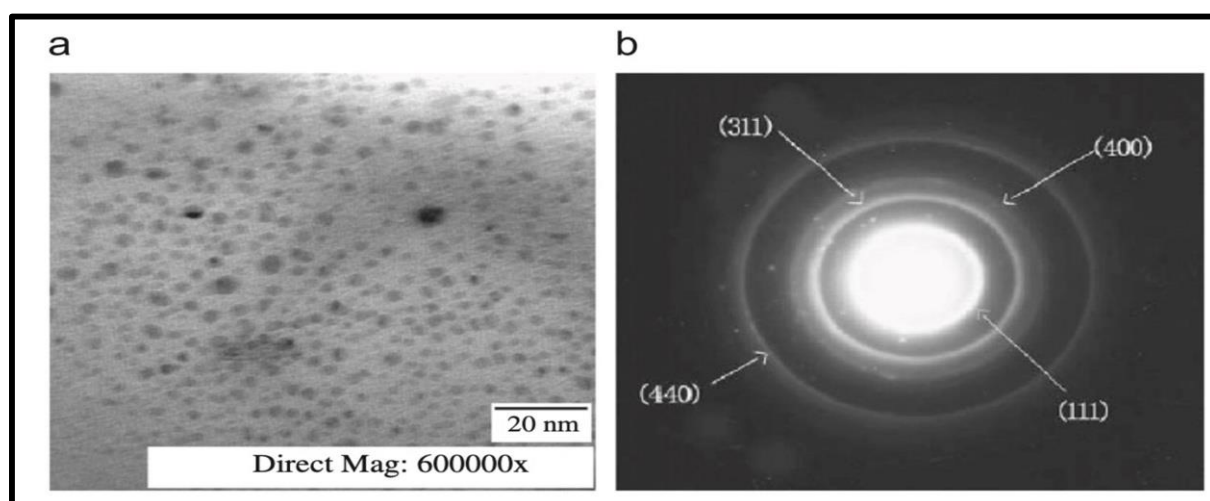


**Figure 6.** TEM images of (a)  $\text{CoFe}_2\text{O}_4\text{/SiO}_2$  (b) electron diffraction pattern (adapted from with the permission from Ref. [106], 2011, *Journal of Magnetism and Magnetic Materials*).

### 2.3.4. Ball-Milling Method

This is a process of creating new alloys and composites from top-down synthesis. It is a low-cost and quick synthesis approach [110]. Milling causes precise deformation because the internal structure of powders is gradually distorted to the nanoscale level.

Gonzalez et al. [111] and Scano et al. [112] synthesized barium ferrite silica and magnetite-silica nanocomposites in molar ratios of 40:60, 50:50, 60:40, 70:30 and silica content of 6, 20, 50 wt %, respectively, by high-energy ball milling. The XRD pattern revealed that a 15 h milling period is sufficient to avoid the formation of hematite phase, but a longer milling period and heat treatment above 900 °C produce hematite phase in BaFe<sub>12</sub>O<sub>19</sub>-SiO<sub>2</sub> and form uniformly distributed spherical narrow (4–6 nm) Fe<sub>3</sub>O<sub>4</sub> nanoparticles in amorphous SiO<sub>2</sub> agglomerate of 100–200 nm in Fe<sub>3</sub>O<sub>4</sub>/SiO<sub>2</sub>. It was discovered that a sample with a compositional ratio of 60 barium ferrite-40 silica milled for 15 h and heated to 900 °C was sufficient to achieve the best magnetic characteristics and excellent dispersion of the hard magnetic phase barium ferrite into the ceramic matrix. In this study, it was found that the value of the highest saturation magnetization and corresponding coercivity (H<sub>c</sub>) for BaFe<sub>12</sub>O<sub>19</sub>-SiO<sub>2</sub> was 43 emug<sup>-1</sup> and 3.4 kOe, respectively.

#### 2.4. Ferrites with Carbon Quantum Dots

Quantum dots are toxic colloidal semiconductors made up of elements from the periodic groups II–VI, III–V, and IV–VI. Carbon has huge potential in nanoelectronics, catalytic supports, drug delivery, sensors and electrochemical energy storage due to its diverse electron orbital types (sp, sp<sup>2</sup>, or sp<sup>3</sup> hybrid) and size-dependent electric and surface properties [113–117]. Carbon quantum dots are a new type of nanomaterial with diameter less than 10 nm. Carbon quantum dots have unique properties compared to conventional semiconductor quantum dots and organic dyes, including intrinsic low toxicity, chemical stability, excellent optical properties, eco-friendliness, biological labelling, bioimaging, sensing, drug delivery, photocatalysis, biomedicines, low cost, and ease of availability [118–120]. The unique and attractive characteristic of CQDs is quantum confinement [121–123]. Properties of CQDs such as surface group and size depend intensively on methods of preparation and applied precursors. Based on the synthesis method, CQDs have different oxygen-, nitrogen-, and sulfur-containing functional groups on the surface [124–126]. The hydrothermal process is a straightforward, low-cost, and widely used method for preparing ferrite nanocomposites with CQDs. A solution of metal salts and a base is autoclaved under pressure in this process, and crystalline structures are formed from the aqueous solution at high vapor pressure. The precipitated precursor suspensions are then placed in a sealed autoclave and slowly cooked at various temperatures and times. The particle size in this process is determined by the rate of hydrolysis and the solubility of metal oxide. High purity, chemical homogeneity, small and consistent particle size, and controlled particle shape are all advantages of this unconventional technique.

The hydrothermal method was used for fabrication of nanocomposites of MFe<sub>2</sub>O<sub>4</sub> (M=Zn, Cu, Co, Ni) with CQDs. CQDs can be prepared from green sources and chemicals such as turmeric, almond, glucose, L-ascorbic acid, lemon peels, etc. Fini et al. [41] and Fini et al. [127] prepared CoFe<sub>2</sub>O<sub>4</sub>-carbon quantum dot and NiFe<sub>2</sub>O<sub>4</sub>-carbon dot nanocomposites using turmeric and almond as green starting material, respectively. From hysteresis loop, the obtained values of saturation magnetization and coercivity of CoFe<sub>2</sub>O<sub>4</sub> and CoFe<sub>2</sub>O<sub>4</sub>-carbon quantum dots were 35 emug<sup>-1</sup> and 585 Oe and 16.8 emug<sup>-1</sup> and 647 Oe, respectively, whereas coercivity of NiFe<sub>2</sub>O<sub>4</sub>-carbon dots rose from 90 Oe to 220 Oe in comparison to pure NiFe<sub>2</sub>O<sub>4</sub>. Increased coercivity of nanocomposites occurred because of increased interactions among nanoparticles. Apparently, magnetic domains are pinned by carbon dots, and as a result, a higher magnetic field is needed for change in magnetic domains of ferrite. In the case of CoFe<sub>2</sub>O<sub>4</sub>-carbon quantum dots, TEM analysis revealed that CQDs were uniform in size from 40 to 100 nm in diameter when prepared for 24 h at 180 °C, when prepared for 48 h at 200 °C, CQDs were uniform from 20 to 100 nm in diameter, and when NiFe<sub>2</sub>O<sub>4</sub>-carbon quantum dots were autoclaved at 180 °C for 6 h, their size was less than 30 nm.

Huang et al. [128] synthesized CQD/ZnFe<sub>2</sub>O<sub>4</sub> nanocomposites using l-ascorbic acid as a source of CQDs and metal nitrates for preparation of metal ferrite. Formation of CQD/ZnFe<sub>2</sub>O<sub>4</sub> nanocomposites was confirmed by TEM. In CQD/ZnFe<sub>2</sub>O<sub>4</sub>, the XRD

pattern revealed no typical CQD peak, which could be attributed to the sample's low concentration and high dispersion of CQDs (Figure 7). The phase structure of  $\text{ZnFe}_2\text{O}_4$  was shown to be unaffected by the inclusion of CQDs during the synthesis. XPS proved the presence of CQDs and revealed the chemical states of synthesized materials for the CQD/ $\text{ZnFe}_2\text{O}_4$  (15 vol %) and  $\text{ZnFe}_2\text{O}_4$  samples. A carbon quantum dot–bismuth ferrite (CQDs/ $\text{BiFeO}_3$ ) heterostructure was developed using glucose as a source of CQDs. Attachment of CQDs on the surface of  $\text{BiFeO}_3$  was confirmed through TEM. Based on XRD analysis, the sites of diffraction peaks of pure  $\text{BiFeO}_3$  powders were similar to those of CQD/ $\text{BiFeO}_3$  composite samples (CQD content: 1.2%, 3.3%, and 4.7%), demonstrating that introducing CQDs to  $\text{BiFeO}_3$  did not modify their crystal structures. As CQD content increased from 1.2% to 4.7%, peaks at  $570\text{ cm}^{-1}$  declined or vanished [129].

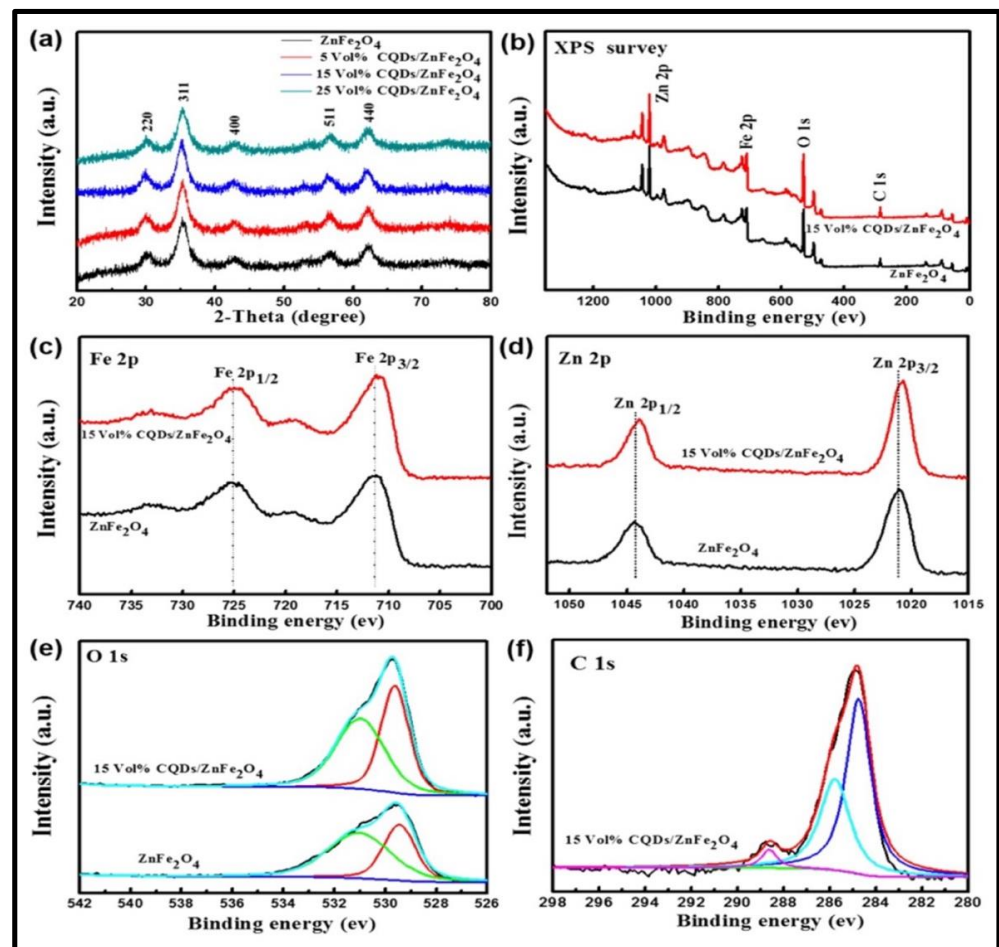
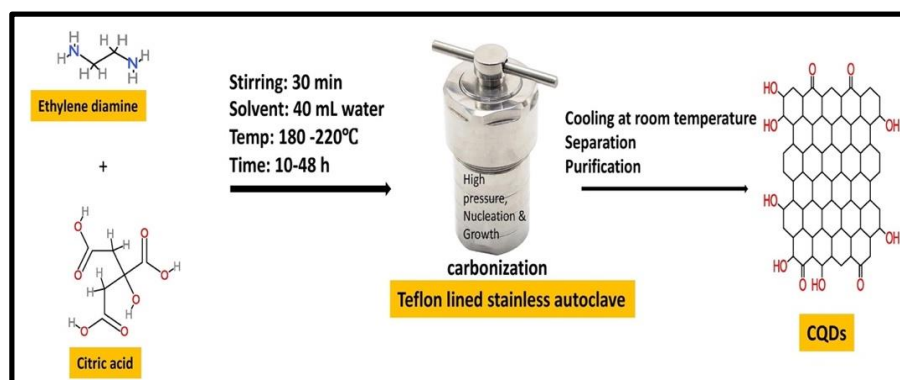


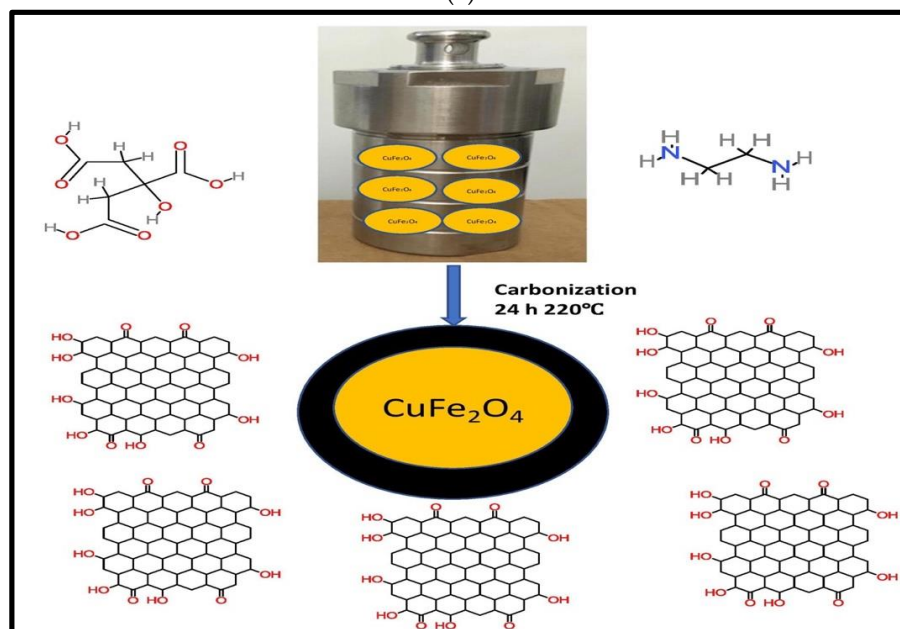
**Figure 7.** (a) XRD patterns of  $\text{ZnFe}_2\text{O}_4$  and CQD/ $\text{ZnFe}_2\text{O}_4$  with different CQDs loading. (b) XPS survey spectra of  $\text{ZnFe}_2\text{O}_4$  and CQD/ $\text{ZnFe}_2\text{O}_4$  (15 vol %). High-resolution XPS spectra of (c) Fe 2p, (d) Zn 2p, (e) O 1s, and (f) C 1s in corresponding samples (adapted from with the permission from Ref. [128], 2017, *Environmental Science and Technology*).

Nabiyouni and Ghanbari [130] reported a  $\text{CuFe}_2\text{O}_4$ –carbon quantum dot nanocomposite as a sensor for detecting Hg (II) Ions. Peaks at  $1630$ ,  $3410$  and  $1050\text{ cm}^{-1}$  in the FTIR spectrum of  $\text{CuFe}_2\text{O}_4$ –carbon quantum dots correspond to presence of C=O, O–H and C–O group in this nanocomposite. SEM of the product confirmed that CQDs were uniform in size around  $50\text{ nm}$  in diameter. From the hysteresis loop of the product, saturation magnetization and coercivity were  $8\text{ emug}^{-1}$  and  $500\text{ Oe}$ , showing ferromagnetic behavior. Figure 8 shows the preparation of (a) CQDs and (b) nanocomposites of copper ferrite–carbon quantum dots by the hydrothermal method. The raw materials used in

the synthesis of ferrites,  $\text{TiO}_2$ ,  $\text{SiO}_2$ , CQDs and their nanocomposites are cheap and easily available. Thus, synthesis of these nanocomposites is cost-effective.



(a)



(b)

**Figure 8.** (a) Method of preparation of CQDs. (b) Schematic of preparation of copper-ferrite carbon quantum dot nanocomposite.

### 3. Applications

Nanotechnology has been a prominent area of research in science and technology for several decades, including space science, medical technology, coatings, and electronics [131]. It is the study and application of structures smaller than 100 nm [132]. Nanotechnology has the potential to revolutionize the coating industry. Nanoscale coatings are attracting a lot of attention around the world. Nanoparticles are being considered as fillers in coatings with changed surface qualities by the paint and coating industries [133]. Nanocoatings are made by mixing nanoparticles (1–100 nm) with coating formulations to improve certain properties. The large surface area and smallness of nanoparticles present many advantages and opportunities to the paint and coating industries [134].

Nanotechnology has been widely applied in medicine, pharmaceuticals, industry, agriculture, and biological sciences, making the 21st century a “golden time” for researchers. Apart from metal and metal oxide nanoparticles, ferrite nanoparticles have raised interest due to their superparamagnetic characteristics and surface area-to-volume ratio, which differ significantly from their bulk counterparts [135]. Ferrites have the advantage of having a bandgap that can absorb visible light, as well as a spinel crystal structure that increases

efficiency by providing additional sites due to the crystal lattice. The bandgap of ferrites is narrower than that of other regularly employed visible light catalysts (Figure 9). The size, shape, and number of substituted transition metal ions can be adjusted to modify the properties of ferrite nanoparticles [136–138]. Doping of spinel ferrites with other metal ions as mixed ferrites is thought to be a useful engineering method for increasing photocatalytic activity and improving the interaction between contaminants and the photocatalytic surface. In recent years, the application of ferrites as a visible light photocatalyst for the decomposition of pollutants in water has attracted much interest.

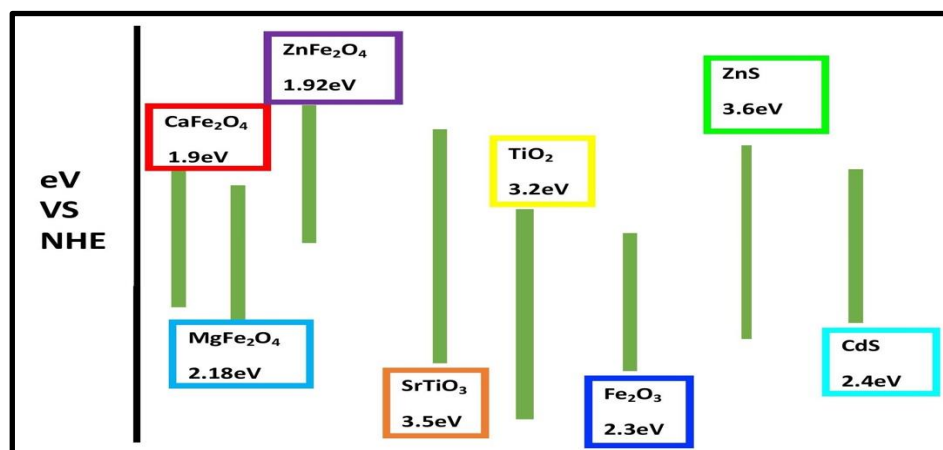


Figure 9. Bandgap energies (eV vs. NHE) for selected ferrites.

In photocatalysis, a semiconductor material interacts with light with higher energy than the bandgap of the semiconductor to excite an electron from the valence band to the conduction band, forming an electron–hole pair, which is responsible for photochemical reactions.

Ferrites have been demonstrated to be effective photocatalysts, generating  $e^-/h^+$  couples on the photocatalyst surface using light energy. The  $e^-/h^+$  pairs are then used for oxidation and reduction reactions, which typically result in the creation of reactive oxygen species such as  $\cdot\text{OH}$  and  $\text{O}_2^-$ , which aid in the breakdown of pollutants (Figure 10). The addition of oxidants such as  $\text{H}_2\text{O}_2$  to the reaction mixture can boost the generation of reactive oxygen species [139].

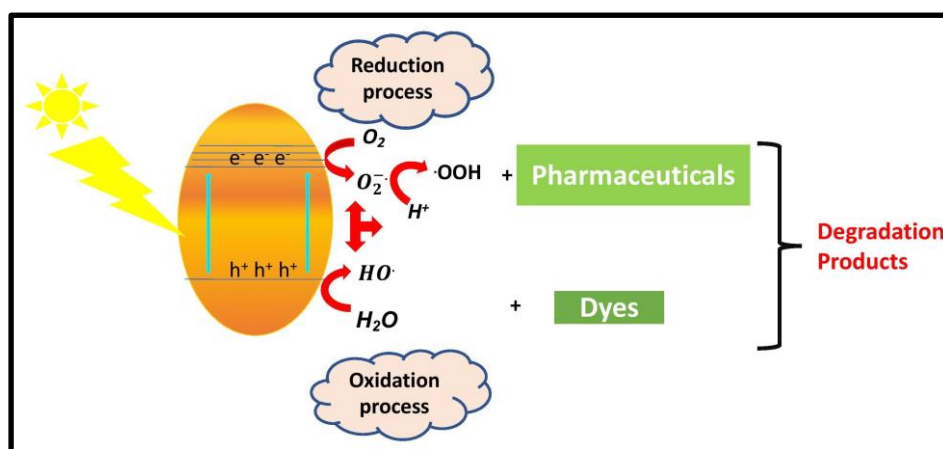
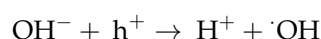
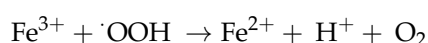


Figure 10. Schematic of reactions occurring via photocatalysis to produce  $\cdot\text{OH}$  to react with contaminants.

When  $\text{H}_2\text{O}_2$  is introduced as an oxidant, iron cations react with  $\text{H}_2\text{O}_2$  according to the processes below.



There is also the possibility that once  $\cdot\text{OOH}$  is formed, it reacts with  $\text{Fe}^{3+}$  to form  $\text{O}_2$ .



The capacity of ferrites to generate  $\cdot\text{OH}$ , which is strongly effective against bacteria, is responsible for its antimicrobial activity. Partial substitution of transition metal in commonly used spinel ferrites improves their antibacterial activity.

For the photocatalytic breakdown of Congo red dye, nanosized iron oxide powder with average crystallite sizes of 35, 100, and 150 nm was utilized. The influence of iron oxide crystal size on the rate of breakdown of Congo red dye was studied both in visible light and in the dark. The results showed that iron oxide particles with crystallite sizes of 35 and 150 nm completely decomposed Congo red dye, whereas iron oxide particles with crystallite sizes of 100 nm were unable to do so [140].  $\text{BaFe}_2\text{O}_4$  was investigated for its visible light photocatalytic activity by decomposition of  $\text{C}_3\text{H}_7\text{OH}$  and  $\text{H}_2\text{O}$ . Ag-doped  $\text{CuFe}_2\text{O}_4$  NPs showed 97% photodegradation of malachite green, whereas  $\text{CuFe}_2\text{O}_4$  degraded only 85% [141]. Table 1 documents the removal of organic pollutants by ferrites [142–147]. Ferrites have been found to be efficient in the disinfection of *E. coli* when coupled with other materials. It has been demonstrated that when ferrites are combined with silver, including Ag/ $\text{MgFe}_2\text{O}_4$  and Ag/ $\text{NiFe}_2\text{O}_4$ , they show antimicrobial activity [148]. Ansari et al. [149] developed chromium-substituted copper ferrite nanoparticles and demonstrated that bacterial growth was inhibited in a size-dependent manner: small nanoparticles possessed strong antibacterial activity, whereas large nanoparticles suppressed bacterial growth at concentrations of more than  $16 \text{ mg/mL}^{-1}$ . The substitution of Co with Cu in cobalt ferrite nanoparticles strongly influenced the microstructure, crystal structure, and particle diameter, and also improved the antibacterial properties and inactivated *E. coli* [17,18,150]. Ferrite photocatalyst-inhibition zones were identical to antibiotic-inhibition zones.

**Table 1.** List of ferrites for removal of pollutants.

S.No.	Ferrites	Preparation Method	Size (nm)	Bandgap (eV)	Crystal Structure	Degradation (%)	References
1.	$\text{Fe}_2\text{O}_3$	Coprecipitation	35	-	cubic	77 (Congo red)	[140]
2.	Codoped $\text{MgFe}_2\text{O}_4$	Hydrothermal	52	1.92	cubic	96.8 (Rhodamine B)	[142]
3.	Doped $\text{MgFe}_2\text{O}_4$	Hydrothermal	96	-	cubic	97.8 (Rhodamine B)	[143]
4.	$\text{CuFe}_2\text{O}_4$	Sol-gel	15	-	cubic	100 (Sulfanilamide)	[144]
5.	$\text{MnFe}_2\text{O}_4$	Sol-gel	281.1	2.8	cubic	90.6 (Norfloxacin)	[145]
6.	$\text{NiFe}_2\text{O}_4$	Coprecipitation	155–185	1.56	cubic	98.5 (Methylene blue)	[146]
7.	$\text{CuFe}_2\text{O}_4$	Solvothermal	150	-	cubic	95 (Phenolic compound)	[147]

The creation of a p–n junction is caused by the connection of semiconductors with distinct bandgaps, which prevents electron–hole recombination and improves their photocatalytic activity (Figure 11). To enhance photocatalytic activity, ferrites have been combined with other photocatalysts, such as TiO<sub>2</sub>, silica, and CQDs. Because of its high photoreactivity, broad-spectrum antibiosis, and chemical stability, TiO<sub>2</sub> is a widely used photocatalyst due to its low cost, abundant availability, biological inertness, photocatalytic stability, and non-toxic behavior toward the environment. It has been used to kill a variety of microorganisms, including bacteria, fungi, and viruses [151–155]. The anatase form of TiO<sub>2</sub> has the best photocatalytic activity, followed by the rutile form. Individual ferrites or TiO<sub>2</sub> alone have lower photocatalytic efficacy than composite photocatalysts when coupled with TiO<sub>2</sub>. Furthermore, when ferrites are added to TiO<sub>2</sub>, the composites become visible light-effective, although TiO<sub>2</sub> alone is only UV light-effective and has a large bandgap (Table 2). A magnetic photocatalyst consisting of a magnetic core covered with a photoactive titanium oxide layer was created to solve the problem of catalyst recovery [13,156–164]. The magnetic core is utilized to improve the photocatalyst’s separation capabilities from the treated water, while the outside titanium oxide layer is employed to degrade organic pollutants.

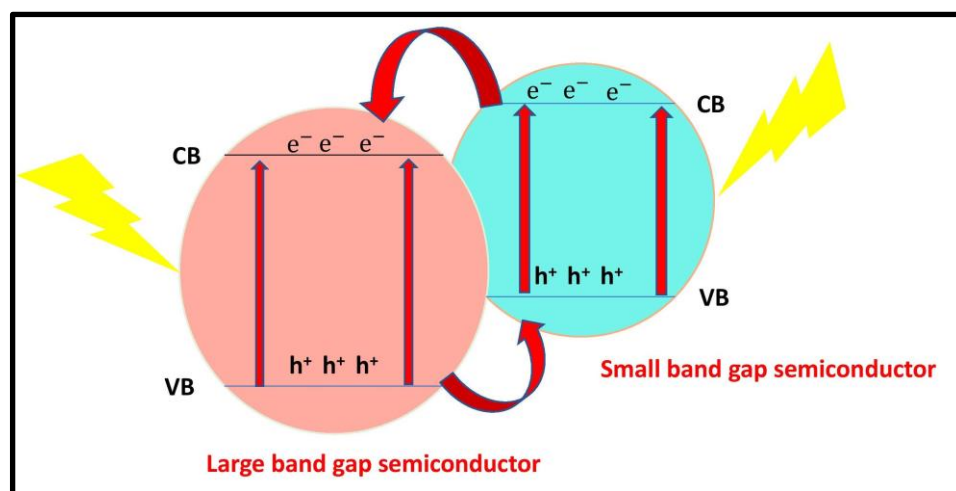
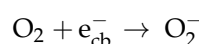


Figure 11. Electron–hole separation in coupled semiconductors.

Table 2. Bandgap of nanocomposites of ferrites with TiO<sub>2</sub>.

S. No.	Nanocomposites of Ferrites with TiO <sub>2</sub>	Bandgap (eV)	References
1.	TiO <sub>2</sub>	3.2	[35]
2.	CoFe <sub>2</sub> O <sub>4</sub> /TiO <sub>2</sub>	2.8	[66]
3.	ZnFe <sub>2</sub> O <sub>4</sub> -TiO <sub>2</sub>	2.3	[74]
4.	TiO <sub>2</sub> /ZnFe <sub>2</sub> O <sub>4</sub>	1.92	[75]
5.	TiO <sub>2</sub> -SrFe <sub>12</sub> O <sub>19</sub>	2.26	[78]
6.	ZnFe <sub>2</sub> O <sub>4</sub> -TiO <sub>2</sub>	1.9	[79]

The mechanism of photocatalysis in doped TiO<sub>2</sub> is shown below:





TiO<sub>2</sub> has bactericidal capabilities due to the high redox potential of surface species produced by photoexcitation, which allows a non-selective oxidative attack on bacteria. Microorganisms were photocatalytically inactivated by reactive oxygen species (ROS) such as hydroxyl radical, superoxide radical (O<sub>2</sub><sup>-</sup>), and hydrogen peroxide (H<sub>2</sub>O<sub>2</sub>) [165,166]. Because the rate of generation of ROS is a function of particle size, crystalline phase, isoelectronic point, BET-specific surface area, aggregate size in suspension solution, and other nanostructural characteristics, the type and source of TiO<sub>2</sub> play an essential role during bacterial inactivation. The presence of a large number of surface hydroxyl groups is the reason for high antibacterial activity. The bactericidal mode of action of ROS depends on the specific microorganisms involved [167,168]. Nanoparticles can interact with microbial cells through a variety of mechanisms, such as by interrupting transmembrane electron transfer, disruption of the cell wall, and oxidizing cell components [169] (Figure 12).

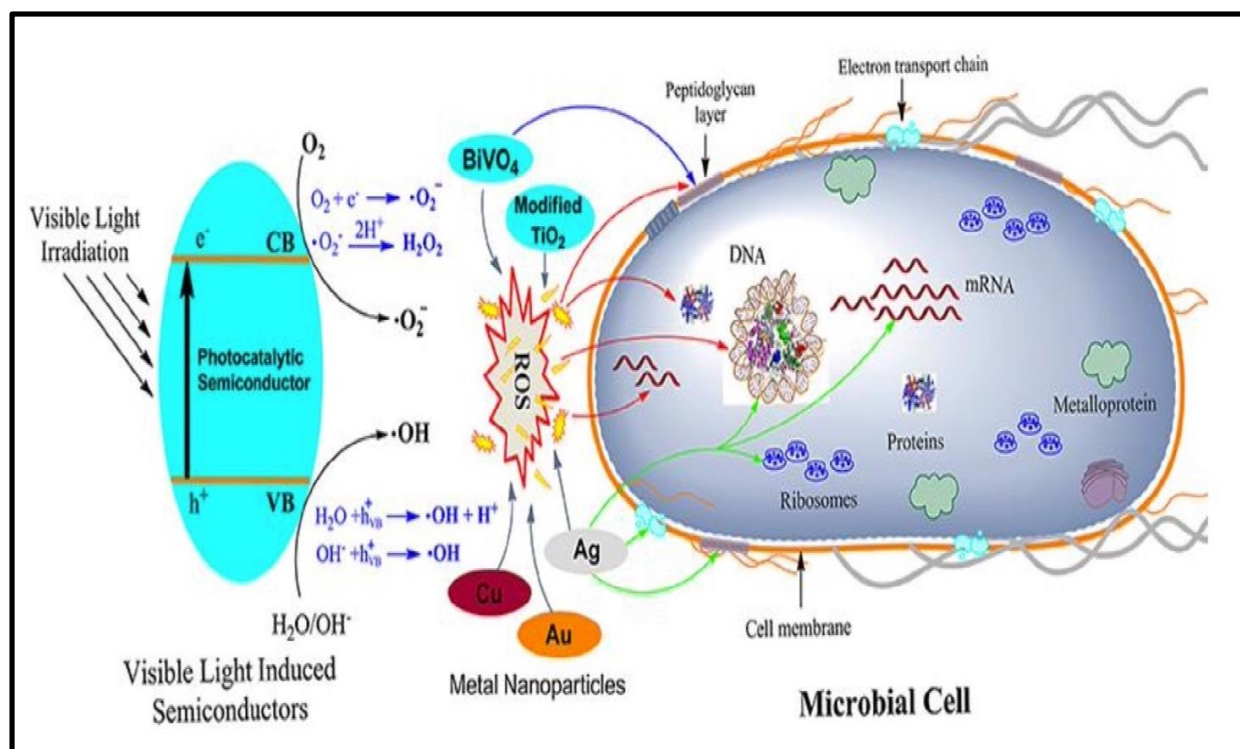


**Figure 12.** Schematic representation of the antimicrobial mechanism proposed for different photocatalytic semiconductors (adapted from with the permission from Ref. [169], 2020, *Materials*).

TiO<sub>2</sub> photocatalytic reactions were used to kill a wide range of bacteria [170]. TiO<sub>2</sub>'s bactericidal and fungicidal activities against *E. coli*, *Staphylococcus aureus*, and *Pseudomonas putida* have been well described [171–173]. Food packaging using TiO<sub>2</sub> coatings or integrated within it has also attracted a lot of interest [174]. Because infection caused by hazardous microbes has become a severe social concern, the development of simple and efficient antibacterial methods and materials is critical. Thus, wood, medical equipment, fabrics, dental implants, architectural materials, and food packaging coated with TiO<sub>2</sub> are efficient for preventing pathogenic infections. Organic dyes such as malachite green,

orange G, rhodamine 6G, amido black 10B, alizarin green, solvent red 23, indigo carmine, methylene blue, and methyl orange [175–179] and pesticides such as 3-tert-butyl-5-chloro-6-methyluracil and 2,4,5-tribromoimidazole were decomposed in the presence of TiO<sub>2</sub> photocatalyst. The degradation of dyes follows pseudo-first-order kinetics according to the Langmuir–Hinshelwood model. It was found that degradation rates and photonic efficiencies were strongly influenced by pH, substrate, photocatalyst concentration and presence of alternative additives, such as H<sub>2</sub>O<sub>2</sub>, KBrO<sub>3</sub>, (NH<sub>4</sub>)<sub>2</sub>S<sub>2</sub>O<sub>8</sub> [180].

Large surface area, easy pore-size management, low cost, rich surface-functional groups, high adsorption capacity, environmental friendliness, and thermal and mechanical stability are all advantages of porous SiO<sub>2</sub> [181–187]. To create well-defined nanocomposites, silica can be used as a support, coating layer, and binding material. When silica coats photocatalysts, it acts as a protective physical barrier, preventing the inside catalysts from dissolving and oxidizing, and therefore improving their chemical stability [188]. Meanwhile, the photocatalyst's surface property can be modified to boost the surface adsorption of reactants. Because pollutant adsorption on photocatalyst surfaces is frequently the rate-determining step for pollutant degradation, large-surface-area photocatalysts are recommended. Furthermore, nanoparticles supported by silica provide more active sites for catalytic reactions. The photocatalytic activity of photocatalysts can be enhanced by these features of silica.

Water solubility, high-emission quantum yields, size-tunable emission, restricted spectral bands, surface modification for a particular sensing application, and photobleaching resistance are advantages of CQDs. Because of high up- and down-converted photoluminescence, electron-transporting and electron-accepting properties, carbon quantum dots have been used as a photocatalyst. The better electron-transporting and electron-accepting capabilities of CQDs will make it easier to separate electron–hole pairs created by solar light radiation, increasing the life of electrons and holes generated by light [189]. These characteristics help CQDs to enhance photocatalytic activity of semiconductors and use solar light. During the process of photocatalysis in nanocomposites of ferrites with CQDs, the electrons agitate from the valence band to the conduction band of ferrites on irradiation of visible light and create holes on the valence band. When CQDs are absent, recombination of electron–hole pairs occurs quickly and O<sub>2</sub><sup>•−</sup> radicals are formed by trapping of electrons by O<sub>2</sub> or by Fe<sup>3+</sup>. Due to their strong electronic conductivity, electrons on the conduction band of ferrites generated by light can be transported to CQDs. These electrons are collected on the CQDs and are absorbed by adsorbed O<sub>2</sub> on the ferrite surface, which results in superoxide radicals (O<sub>2</sub><sup>•−</sup>). These radicals play an important role during photocatalysis [128] (Figure 13).

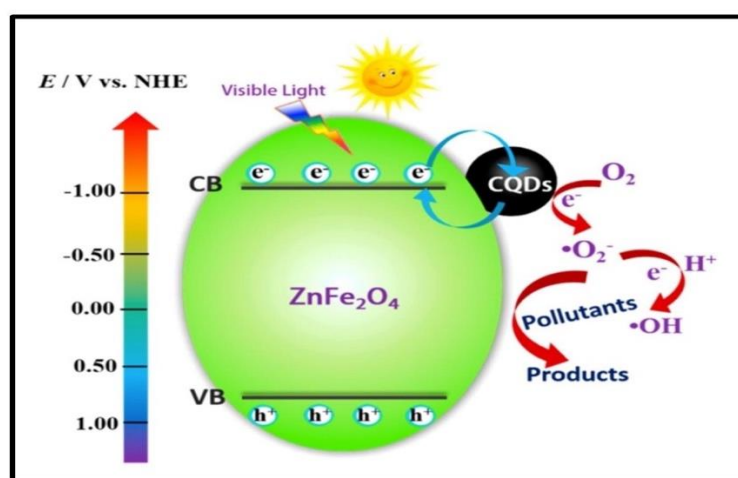


**Figure 13.** Schematic of separation and transfer of photogenerated charges in CQD/ZnFe<sub>2</sub>O<sub>4</sub> nanocomposite (adapted from with the permission from Ref. [128], 2017, *Environmental Science and Technology*).

CQDs' inhibitory effect on microorganisms is mediated by three molecular mechanisms (Figure 14):

- (1) Cell membranes and cell walls are destroyed.
- (2) The release of reactive oxygen species (ROS) in order to kill the cells.
- (3) Inhibiting cell proliferation by interacting with nucleic material (DNA/RNA).

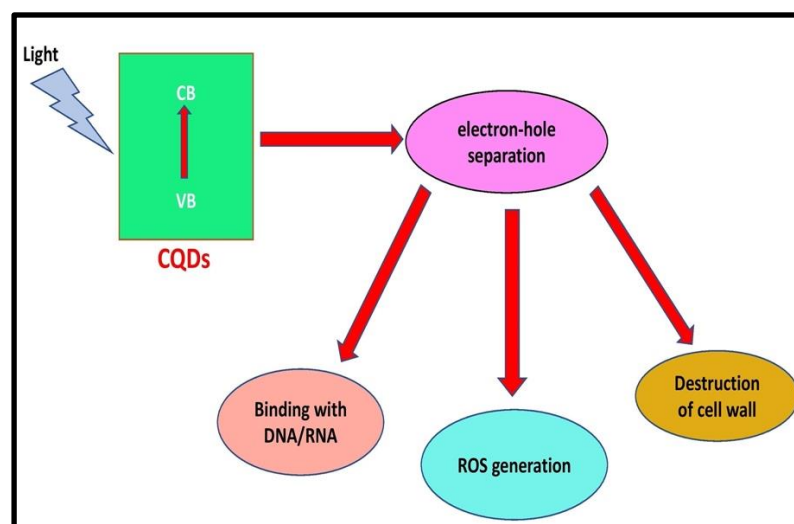


**Figure 14.** The inhibitory action of CQDs on microbial organisms mainly takes place via three molecular mechanisms.

CQDs produce a significant number of free electrons and holes due to strong electron transport. Excessive free radicals, such as hydroxide anions ( $\text{OH}^-$ ), superoxide singlet oxygen ( $\text{O}_2^-$ ), triplet oxygen, and per-hydroxyl anions, are produced by photoactivated CQDs. The buildup of reactive oxygen species (ROS) inside the cell hinders respiration and replication, resulting in microbial cell death [190]. When illuminated by light, CQDs operate as conductive nanoscaffolds, and they are used in nanocomposites of ferrite with CQDs to overcome hematite's short hole diffusion length and low hole mobility limit. As a result, a large number of holes can drift towards the nanocomposite surface, generating a huge number of ROS at the surface. As a result, antibacterial activity improves [191].

### 3.1. Photocatalytic Applications for Degradation of Organic Compounds

Extreme pollution of water bodies is a severe risk to both human beings and other life forms. Water contaminated with organic compounds such as pharmaceuticals, dyes, heavy-metal ions, and pesticides has received scientific attention because of its dangerous constituents, and it is necessary to treat to secure environmental safety [192,193]. Of several AOPs, semiconductor-based photocatalysis is a successful and low-cost technique for the treatment of water contaminants and microbes. In photocatalysis, clean and inexhaustible solar energy is converted into useful chemical forms, and all photocatalytic reactions advances through relatively green conditions [194–198]. In this method, complete degradation of organic compounds to  $\text{H}_2\text{O}$  and  $\text{CO}_2$  occurs, and no secondary pollutants are generated.

The influence of doping of Ni/Co and Eu on  $\text{Fe}_3\text{O}_4/\text{TiO}_2$  magnetic core-shell nanocomposites were investigated by degradation of amlodipine [199] and rhodamine B [200] under ultraviolet light irradiation, respectively. It was observed that factors playing a necessary role in decomposition of amlodipine are weight percentage, number of dopants, calcination time, calcination temperature and pH of the amlodipine. Jiang et al. [81] reported that the  $M_s$  value of  $\text{TiO}_2$ -coated  $\text{Fe}_3\text{O}_4$  (14 emu/g) is much lower than that of bare  $\text{Fe}_3\text{O}_4$  (63 emu/g). The decrease in saturation magnetization is mainly due to the non-magnetic  $\text{TiO}_2$  content in the nanocomposites. and has strong photocatalytic activity for photodegradation of rhodamine B solution. Titania-coated magnetite ( $\text{Fe}_3\text{O}_4/\text{TiO}_2$ ) nanocubes showed

excellent efficiency for degradation of methylene blue, and this efficiency was further promoted by addition of hydrogen peroxide within only 5 min of reaction time in the absence of UV irradiation. Even after recycling the sample six times, the introduced catalyst was found to retain as much as 90% initial efficiency [201]. Xu et al. [74] studied the degradation of methylene blue and methyl orange using visible light-active  $\text{TiO}_2/\text{ZnFe}_2\text{O}_4$  photocatalysts. The light-absorbing semiconductor  $\text{ZnFe}_2\text{O}_4$  and the wide-bandgap titanium oxide created a linked semiconductor system in the  $\text{TiO}_2/\text{ZnFe}_2\text{O}_4$  photocatalyst, resulting in efficient primary charge separation and photocatalytic activity under visible light irradiation. The influence of calcination temperature and  $\text{ZnFe}_2\text{O}_4$  quantity on  $\text{TiO}_2/\text{ZnFe}_2\text{O}_4$  photocatalytic activity was also studied. Golshana et al. [202] reported  $\text{TiO}_2@\text{CuFe}_2\text{O}_4$  as photocatalyst for decomposition of 2,4-dichlorophenoxyacetic acid (2,4-D). Over 97.2% of 2,4-D was degraded within 60 min at 0.3 mM PMS and 0.1 g/L. Difference in energy levels of  $\text{CuFe}_2\text{O}_4$  and  $\text{TiO}_2$  prevents electron–hole recombination, thus improving photocatalytic activity (Figure 15).

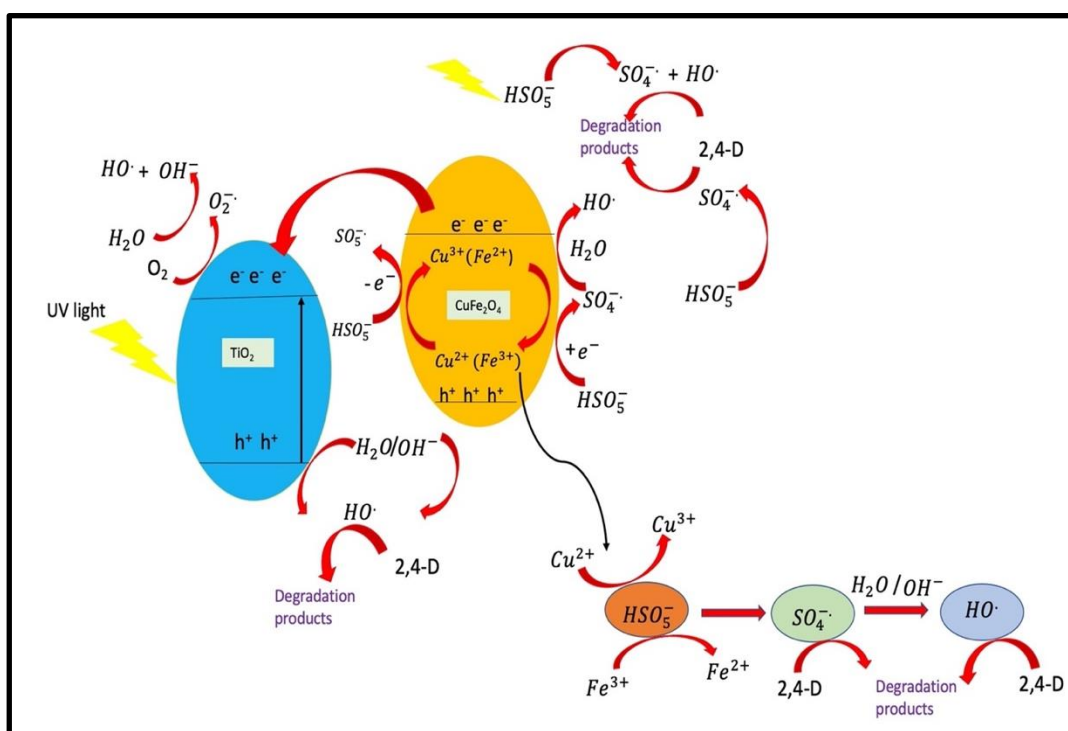


**Figure 15.** Mechanism of degradation of 2,4-D by  $\text{TiO}_2@\text{CuFe}_2\text{O}_4$  nanocomposites.

The photocatalytic activity of  $\text{NiFe}_2\text{O}_4@\text{TiO}_2/\text{Pt}$  nanocomposites was demonstrated by degradation of methyl orange and acid brown in an aqueous solution under irradiation with UV light. Maximum wavelengths of methyl orange and acid brown were degraded about 45% and 65% in 90 min under ultraviolet light and in the presence of magnetic photocatalyst [203]. Aziz et al. [87] used a nanocomposite of  $\text{TiO}_2$  with  $\text{SrFe}_{12}\text{O}_{19}$  as photocatalyst for degradation of a recalcitrant phenolic compound (2,4-dichlorophenol) under illumination of daylight. Under stronger sunlight illuminance, 2,4-DCP (50 mg/L) was degraded completely in 120 min (supported photocatalyst) and 180 min (unsupported  $\text{TiO}_2$ ). Under diffused sunlight, 100% decomposition of 2,4-DCP was accomplished in 240 min for the supported  $\text{TiO}_2$  and 90% decomposition in 300 min for the unsupported  $\text{TiO}_2$ .

Haw et al. [85] found that in  $\text{CoFe}_2\text{O}_4/\text{TiO}_2$  nanocatalysts, the presence of  $\text{Co}^{2+}$  and  $\text{Fe}^{3+}$  ions in oxide form on the surface of  $\text{TiO}_2$  led to visible light absorption in the wavelength range 550–650 nm. The photocatalytic degradation of reactive red 120 was studied by varying its concentration and amount of nanocatalyst in order to attain maximum degra-

gradation. The role of electron acceptors in photocatalytic degradation of RR 120 was studied in the presence of a magnetic nanocatalyst. In comparison to commercial rutile phase  $\text{TiO}_2$  and pure urchin-like  $\text{TiO}_2$  microparticles, the  $\text{CoFe}_2\text{O}_4$ -3D  $\text{TiO}_2$  nanocomposites demonstrated improved photodegradation of methylene blue due to a decreased recombination rate of photoexcited charge carriers [204]. Bavarsiha et al. [205] and Chen et al. [206] studied the degradation of methylene blue by  $\text{SrFe}_{12}\text{O}_{19}/\text{SiO}_2/\text{TiO}_2$  and  $\text{TiO}_2/\text{SiO}_2/\text{Ni-Cu-Zn}$  ferrite composites, respectively. Photodegradation of methylene blue was 80% in the presence of  $\text{SrFe}_{12}\text{O}_{19}/\text{SiO}_2/\text{TiO}_2$  at irradiation time of 180 min and 83.9% in the presence of  $\text{TiO}_2/\text{SiO}_2/\text{Ni-Cu-Zn}$  ferrite composite after 6 h Xe arc lamp irradiation.  $\text{ZnFe}_2\text{O}_4/\text{TiO}_2$  heterojunction was used for the removal of bisphenol A. The close heterojunction interface between p-type  $\text{ZnFe}_2\text{O}_4$  and n-type  $\text{TiO}_2$  can promote charge transfer more easily, resulting in lower  $e^- - h^+$  pair recombination efficiency and higher visible light-responsive photocatalytic activity in  $\text{ZnFe}_2\text{O}_4$  heterostructure [93]. Figure 16 shows the mechanism of photodegradation of bisphenol A by  $\text{ZnFe}_2\text{O}_4/\text{TiO}_2$  heterojunction. Path 1 represents the excitation of  $e^-$  from the VB of  $\text{ZnFe}_2\text{O}_4$  to CB to produce an  $e^- - h^+$  pair. Path 2 represents the transfer of excited  $e^-$  in  $\text{ZnFe}_2\text{O}_4$  across the interface of nanocomposites to the CB of anatase  $\text{TiO}_2$ , and leave holes in the VB of  $\text{ZnFe}_2\text{O}_4$ . It reduces the recombination rate of holes and electrons. Path 3 indicates that photogenerated holes in VB of  $\text{ZnFe}_2\text{O}_4$  can decompose bisphenol A under visible light irradiation, and  $e^-$  in the VB of  $\text{TiO}_2$  can react with  $\text{O}_2$  to generate  $\text{O}_2^{\cdot -}$  and  $\cdot\text{OOH}$  radicals (Path 4 and 5). The formed radicals can react with electrons and protons to form  $\cdot\text{OH}$  (hydroxyl radicals) (Path 6). Coromelci et al. [207] developed  $\text{TiO}_2/\text{ZnFe}_2\text{O}_4$  and  $\text{TiO}_2/\text{ZnFe}_{1.98}\text{La}_{0.02}\text{O}_4$  heterostructures for the degradation of methylene blue. Photocatalytic degradation of 97%, 91% and 70% was achieved using  $\text{TiO}_2/\text{ZnFe}_{1.98}\text{La}_{0.02}\text{O}_4$  under UV light, sunlight, and visible light.

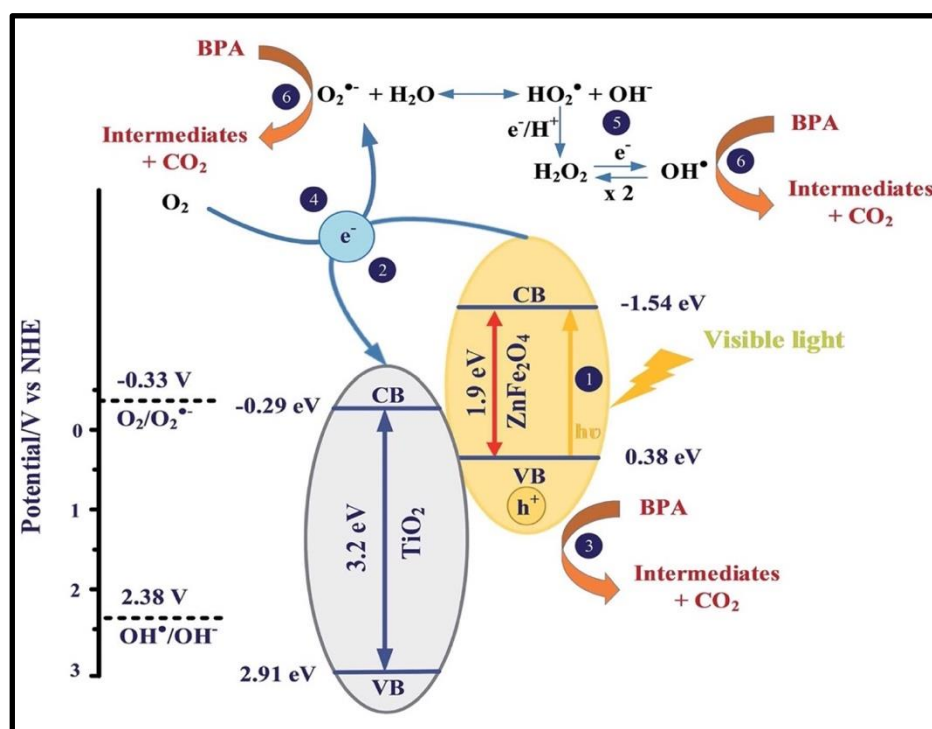


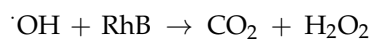
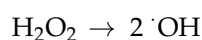
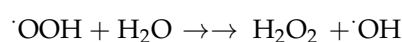
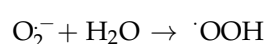
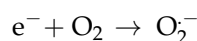
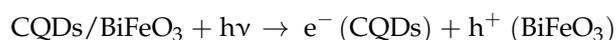
**Figure 16.** Mechanism of degradation of bisphenol A by  $\text{ZnFe}_2\text{O}_4/\text{TiO}_2$  heterojunction (adapted from with the permission from Ref. [93], 2017, *the Royal Society of Chemistry*).

Photocatalytic property of  $\text{CoFe}_2\text{O}_4$ -carbon quantum dot nanocomposites under ultraviolet irradiation was evaluated by degradation of three azo dyes (acid black 24, acid brown 14 and acid red 1). It was observed that the degradation of acid brown 14, acid black 24 and acid red 1 was 90%, 95%, and 60% at 90, 60, and 120 min, respectively [41].

Yakob et al. [108] developed  $\text{CoFe}_2\text{O}_4$  and  $\text{CoFe}_2\text{O}_4/\text{SiO}_2$  and evaluated its photocatalytic activity against methylene blue. The  $\text{CoFe}_2\text{O}_4/\text{SiO}_2$  nanocomposites showed a lower optical bandgap than bare  $\text{CoFe}_2\text{O}_4$  due to a smaller surface defect and greater particle size. Because of the silica coating on  $\text{CoFe}_2\text{O}_4$ ,  $\text{CoFe}_2\text{O}_4/\text{SiO}_2$  had higher photocatalytic activity than  $\text{CoFe}_2\text{O}_4$ . Methylene blue photodegradation rate reached 80.6%.

A novel CQDs/ $\text{ZnFe}_2\text{O}_4$  composite showed a strong transient photocurrent response, which was much higher than  $\text{ZnFe}_2\text{O}_4$ , thus indicating better transfer and separation efficiency of photogenerated electron–hole pairs. During the photocatalysis process, CQDs serve as an electron reservoir, a transporter, and a strong energy transfer component. An ESR study found that reactive species contributing towards removal of NO were  $\text{O}_2^-$  and  $\cdot\text{OH}$  [128]. The photocatalytic activities of pure  $\text{BiFeO}_3$ , CQDs and CQDs/ $\text{BiFeO}_3$  composite were investigated against rhodamine B. Due to formation of a heterojunction at the interface between CQD and  $\text{BiFeO}_3$  and electron-accepting properties of CQDs, the pure  $\text{BiFeO}_3$  had the poorest photocatalytic activity compared to CQDs and CQDs/ $\text{BiFeO}_3$ . The sample with 3.3 wt % of CQDs in CQDs/ $\text{BiFeO}_3$  composite had the highest photocatalytic activity, and as a content of CQDs exceeded 3.3 wt %, the photocatalytic activity decreased because too much CQDs covered the surface of  $\text{BiFeO}_3$  and reduced the adsorption of  $\text{O}_2$  [129]. Mesoporous silica nanoparticles loaded with different amounts of  $\text{Fe}_2\text{O}_3$  nanoparticles synthesized by the sol–gel method was used for the degradation of methylene blue and Congo red dye. Best results were obtained with 20% weight loading of hematite nanoparticles, indicating less agglomeration and availability of more catalytic sites [208]. Titanium-substituted  $\text{SrFe}_2\text{O}_4$  and  $\text{MgFe}_2\text{O}_4$  nanoparticles were used for the removal of nitroaromatic compounds and rhodamine B dye [209,210].  $\text{Sr}_{0.4}\text{Ti}_{0.6}\text{Fe}_2\text{O}_{4.6}$  @  $\text{SiO}_2$  nanocomposites removed 96% of pendimethalin [211].

The mechanism of rhodamine B degradation by CQDs/ $\text{BiFeO}_3$  heterojunction is shown below:



### 3.2. Photocatalytic Applications for Degradation of Microbes

Bacterial infectious illnesses have long posed a severe threat to human health, and treating them has always been a risk for medical personnel. Antimicrobial resistance (AMR) has emerged as a serious threat to the successful treatment of bacterial illnesses in the last 70 years or more as a result of widespread antibiotic usage. Misuse of antibiotics results in increase and spread of resistant pathogens. Antibiotic-resistant illnesses affect more than 2.8 million individuals in the United States each year, resulting in around 35,000 fatalities [212]. It is projected that by 2050, AMR will cause 10 million deaths per year, costing \$100 trillion [213]. MSNs are ideally suited for targeted drug delivery due to their flexible and desired features, such as high drug loading capacity, adjustable pore size and volume, ease of functionalization, and biocompatibility. Silica nanoparticles have a

lot of silanol groups (Si-OH) on their surfaces, which can be easily controlled as a surface probe attachment site.

The antibacterial behavior of  $\text{NiFe}_2\text{O}_4/\text{TiO}_2/\text{Pt}$  nanocomposites was evaluated using degradation of *E. coli* bacteria. It was found that nanocomposites had a feasible magnetic feature for easy separation and effective photocatalytic properties. As time increased, more bacteria were degraded on the catalyst [203]. Atacan et al. [92] demonstrated the antibacterial activity of  $\text{ZnFe}_2\text{O}_4/\text{Ag-TiO}_2$  nanocomposite against Gram-positive bacteria (*S. aureus*) and Gram-negative bacteria (*E. coli*). The degradation rate of *S. aureus* was higher than *E. coli*. The inhibition diameter of  $15 \pm 0.2$  mm for  $\text{ZnFe}_2\text{O}_4/\text{Ag-TiO}_2$  nanocomposite was also measured, since the antibacterial activity increased with nanocomposite formation.

To create photokilling agents, Chen et al. [214] utilized two unique properties of titania: its photocatalytic activity and its capacity to self-assemble dopamine onto its surface. The  $\text{Fe}_3\text{O}_4/\text{TiO}_2$  nanocomposites had photocatalytic activity as well as the ability to target bacteria, in addition to their magnetic characteristics. The  $\text{IgG-Fe}_3\text{O}_4/\text{TiO}_2$  nanocomposite was shown to be efficient at inhibiting the cell development of various harmful bacteria when exposed to UV radiation. The photokilling capabilities of synthesized nanocomposites were evaluated using antibiotic-resistant bacterial strains, such as multiantibiotic-resistant *S. pyogenes*, methicillin-resistant *Staphylococcus aureus* (MRSA), *Staphylococcus saprophyticus*, and *Streptococcus pyogenes*. The antibacterial activity of  $\gamma\text{-Fe}_2\text{O}_3/\text{SiO}_2/\text{TiO}_2\text{-Ag}$  nanocomposites was investigated by Cui et al. [215]. It was demonstrated that the introduction of silver nanoparticles into the  $\text{TiO}_2$  matrix facilitates charge separation by trapping photogenerated electrons, thereby enhancing biological activity and photoactivity.

The antibacterial effect of  $\text{NiFe}_2\text{O}_4$ -carbon quantum dots nanocomposite was investigated by degradation of *Pseudomonas aeruginosa* bacteria. It was found that as time increases, more bacteria were degraded on nanocomposites [127]. Yang et al. [216] found that CQD adsorption causes bacterial cell surface destruction, since the CQDs may change the charge balance of the bacterial surface and can insert into the bacterial surface via the long alkyl chains, which ultimately leads to the inactivation of Gram-positive bacteria. Moradlou et al. [217] (Figure 17) grew thin films of CQD-incorporated hematite ( $\text{CQDs}/\alpha\text{-Fe}_2\text{O}_3$ ) and nanostructured hematite ( $\alpha\text{-Fe}_2\text{O}_3$ ) on titanium substrate. Under dark and light circumstances, the antibacterial activity of the produced sample was tested against Gram-negative (*E. coli*) and Gram-positive (*S. aureus*) bacteria. It was observed that antimicrobial activity of the samples was less in the dark than under light illumination. The antimicrobial investigation revealed that  $\alpha\text{-Fe}_2\text{O}_3$  and  $\text{CQDs}/\alpha\text{-Fe}_2\text{O}_3$  were toxic to the chosen microbe, and that samples ( $\text{Ti}/\alpha\text{-Fe}_2\text{O}_3$ ,  $\text{Ti}/\text{CQDs}/\alpha\text{-Fe}_2\text{O}_3$ ) have higher antibacterial activity against *S. aureus* than *E. coli*, owing to the existence of an additional layer in the outer membrane of *E. coli*. The mechanism of bactericidal activity was the entrance of iron cation into the bacterial cell via its membrane and the formation of reactive oxygen species.

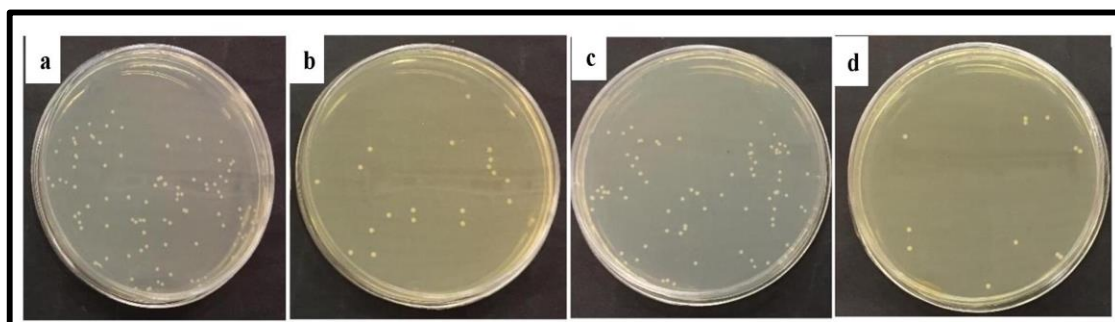


**Figure 17.** Colonies growing on agar plates for samples  $\text{Ti}/\alpha\text{-Fe}_2\text{O}_3$  (a,b) and  $\text{Ti}/\text{CQD}/\alpha\text{-Fe}_2\text{O}_3$  (c,d) against *E. coli* (a,c) and *S. aureus* (b,d) bacterial strains (adapted from with the permission from Ref. [217], 2019, *Journal of Photochemistry and Photobiology A: Chemistry*).

A silver-deposited silanized cobalt ferrite composite ( $\text{CoFe}_2\text{O}_4/\text{SiO}_2/\text{Ag}$ ) was produced and impregnated with streptomycin antibiotic by Kooti et al. [218]. Disk diffusion was used to investigate the antibacterial activity of  $\text{CoFe}_2\text{O}_4/\text{SiO}_2/\text{Ag}$  alone and in combination with streptomycin against Gram-positive and Gram-negative bacteria. The bactericidal effect of this compound was found to be increased when combined with streptomycin based on the diameter of inhibition zones. It was demonstrated that the bactericidal activity of  $\text{CoFe}_2\text{O}_4/\text{SiO}_2/\text{Ag}$  in combination with streptomycin against all test stains was higher than each of  $\text{CoFe}_2\text{O}_4/\text{SiO}_2/\text{Ag}$  and streptomycin applied alone. The DIZ values for streptomycin-impregnated  $\text{CoFe}_2\text{O}_4/\text{SiO}_2/\text{Ag}$  composite were 19, 17, 15, and 14 mm for *B. subtilis*, *E. coli*, *S. aureus*, and *Pseudomonas aeruginosa*, respectively, using a composite concentration of  $10 \text{ mg/mL}^{-1}$ . A summary of applications of nanocomposites of ferrites with  $\text{TiO}_2$ , silica and CQDs for removal of pollutants is given in Tables 3 and 4.

**Table 3.** List of ferrites and their nanocomposites with  $\text{TiO}_2$ , Silica and CQDs for removal of pollutants.

S.No.	Photocatalyst	Pollutant	Degradation (%)	Time (min)	Light Source	References
1.	$\text{CoFe}_2\text{O}_4$ -CQD	Acid black 24, acid brown 14, acid red 1	95, 90, 65	60, 90, 120	UV	[41]
2.	$\text{CoFe}_2\text{O}_4$ - $\text{TiO}_2$	Reactive red 120	98.89	360	UV	[85]
3.	$\text{TiO}_2/\text{SrFe}_{12}\text{O}_{19}$	2,4-dichlorophenoxyacetic acid	100	240	sunlight	[87]
4.	$\text{CoFe}_2\text{O}_4/\text{SiO}_2$	Methylene blue	80.6	120	UV	[108]
5.	CQD/ $\text{BiFeO}_3$	Rhodamine B	-	60	Visible	[129]
6..	$\text{Ni}/\text{Co}-\text{Fe}_3\text{O}_4/\text{TiO}_2$	Amlodipine drug	92.49	90	UV	[198]
7.	$\text{Fe}_3\text{O}_4/\text{TiO}_2$ : Eu	Rhodamine B	85.3	180	Visible	[199]
8.	$\text{Fe}_3\text{O}_4/\text{TiO}_2$	Methylene blue	81	6	UV	[201]
9.	$\text{TiO}_2@\text{CuFe}_2\text{O}_4$	2,4-dichlorophenoxyacetic acid	69.7	60	UV	[202]
10.	$\text{NiFe}_2\text{O}_4@\text{TiO}_2/\text{Pt}$	Methyl orange, acid brown	45, 65	90	UV	[203]
11.	$\text{SrFe}_{12}\text{O}_{19}/\text{SiO}_2/\text{TiO}_2$	Methylene blue	80	180	UV	[205]
12.	$\text{TiO}_2/\text{SiO}_2/\text{Ni}-\text{Cu}-\text{Zn}$ ferrite	Methylene blue	83.9	360	Visible	[206]
13.	$\text{Fe}_2\text{O}_3/\text{SiO}_2$	Methylene blue and congo red	88, 88	180, 240	Visible	[208]
14.	$\text{Sr}_{1-x}\text{Ti}_x\text{Fe}_2\text{O}_{4+\delta}$	p-nitrophenol, pendimethalin, martius yellow	91.3, 94.4, 87.2	120	Visible	[209]
15.	$\text{Mg}_{1-x}\text{Ti}_x\text{Fe}_2\text{O}_{4+\delta}$	Rhodamine-B	98	120	Visible	[210]
16.	$\text{Sr}_{0.4}\text{Ti}_{0.6}\text{Fe}_2\text{O}_{4.6}@\text{SiO}_2$	pendimethalin	96	120	Visible	[211]
17.	$\gamma\text{-Fe}_2\text{O}_3@\text{SiO}_2@\text{TiO}_2\text{-Ag}$	Methyl orange	84	60	UV	[215]

**Table 4.** List of various nanocomposites of ferrites with  $\text{TiO}_2$ , silica and CQDs for removal of microbes.

S. No.	Photocatalyst	Microbes	Degradation	Light Source	References
1.	$\text{ZnFe}_2\text{O}_4/\text{Ag}-\text{TiO}_2$	<i>S. aureus</i> , <i>E. coli</i>	Zone of inhibition $15 \pm 0.2$ , $12 \pm 0.3$ mm respectively	Dark	[92]
2.	Ig-G- $\text{Fe}_3\text{O}_4/\text{TiO}_2$	<i>Staphylococcus saprophyticus</i> , <i>Streptococcus pyogenes</i> , <i>S. aureus</i>	79.15%, 82.87% 82.40%	-	[214]
3.	$\gamma\text{-Fe}_2\text{O}_3@\text{SiO}_2@\text{TiO}_2\text{-Ag}$	<i>E. coli</i>	75%, 97%	Dark, visible	[215]
4.	Ti/CQD@hematite	<i>S. aureus</i> , <i>E. coli</i>	70%, 20% 80%, 35%	Dark, Visible	[217]
5.	$\text{CoFe}_2\text{O}_4/\text{SiO}_2/\text{Ag}$	<i>S. aureus</i> , <i>Bacillus subtilis</i> , <i>E. coli</i> , <i>Pseudomonas aeruginosa</i>	Diameter of inhibition zone 20, 21, 17, 18 mm respectively	-	[218]

#### 4. Challenges and Opportunities

Exploring synthetic ways for low-cost large-scale production is essential for the wide use of nanotechnology. The large-scale production of these nanocomposites with uniform and high quality is still a challenging task. There is still a lot of work to be done for synthesis and optimizing the materials for a wide range of applications, and it is critical to assess the toxicity and environmental issues of nanocomposites. Nanocomposites exhibit distinct qualities, such as a high surface area-to-volume ratio, a significant number of reactive sites available to enable the dispersal of organic pollutants on the surface and pores, tininess, and high recovery capacity. High surface area-to-volume ratio property of nanocomposites controls the interactions with bacteria and pollutants. These characteristics provide new opportunities for numerous applications in photocatalysis. Comparative studies on change in the cocatalyst viz.  $\text{TiO}_2$ ,  $\text{SiO}_2$ , and CQDs on the photocatalytic activity of ferrites needs to be addressed.

#### 5. Conclusions

Nanocomposites of ferrites with  $\text{TiO}_2$ ,  $\text{SiO}_2$ , and CQDs are presently being used for environment protection. In this review, methods of preparation, such as coprecipitation, sol-gel, hydrothermal, solvothermal, and Stöber, structural features and photocatalytic activity of nanocomposites of ferrites with  $\text{TiO}_2$ ,  $\text{SiO}_2$ , and CQDs for removal of various toxicants such as dyes, heavy-metal ions, pharmaceuticals, and microbes have been discussed. Mechanisms associated with their applications have also been addressed. Such nanocomposites have become a subject of great scientific interest due to their physiochemical properties, such as thermal stability, tunable shape and size, chemical stability, excellent magnetic characteristics, cost-effectiveness and large surface area. These nanocomposites possess more photocatalytic activity than individual moieties. Among various nanocomposites, nanocomposites of ferrites with CQDs show more photocatalytic activity due to their excellent sunlight-harvesting ability, up-conversion photoluminescence, tunable photoluminescence (PL), and effective promotion of electron-hole separation rate.

**Author Contributions:** Writing-original draft preparation, A.K. and M.K.; Writing-review and editing, A.K., M.K., P.V. and V.S. All authors have read and agreed to the published version of the manuscript.

**Funding:** This research received no external funding.

**Institutional Review Board Statement:** Not applicable.

**Informed Consent Statement:** Not applicable.

**Data Availability Statement:** Not applicable.

**Conflicts of Interest:** The authors declare no conflict of interest.

#### References

1. World Health Organization. Drinking Water. 2019. Available online: <https://www.who.int/news-room/fact-sheets/detail/drinking-water> (accessed on 27 March 2019).
2. Asfaram, A.; Ghaedi, M.; Goudarzi, A.; Hajati, S. Ultrasound-Assisted Binary Adsorption of Dyes onto Mn@ CuS/ZnS-NC-AC as a Novel Adsorbent: Application of Chemometrics for Optimization and Modeling. *J. Ind. Eng. Chem.* **2017**, *54*, 377–388. [[CrossRef](#)]
3. Chung, K.-T. Azo Dyes and Human Health: A Review. *J. Environ. Sci. Health C* **2016**, *34*, 233–261. [[CrossRef](#)] [[PubMed](#)]
4. Zhou, Y.; Lu, J.; Zhou, Y.; Liu, Y. Recent Advances for Dyes Removal Using Novel Adsorbents: A Review. *Environ. Pollut.* **2019**, *252*, 352–365. [[CrossRef](#)] [[PubMed](#)]
5. Ojemaye, M.O.; Okoh, A.I. Multiple Nitrogen Functionalized Magnetic Nanoparticles as an Efficient Adsorbent: Synthesis, Kinetics, Isotherm and Thermodynamic Studies for the Removal of Rhodamine B from Aqueous Solution. *Sci. Rep.* **2019**, *9*, 9672. [[CrossRef](#)] [[PubMed](#)]
6. Mazaheri, H.; Ghaedi, M.; Ahmadi Azghandi, M.H.; Asfaram, A. Application of Machine/Statistical Learning, Artificial Intelligence and Statistical Experimental Design for the Modeling and Optimization of Methylene Blue and Cd(II) Removal from a Binary Aqueous Solution by Natural Walnut Carbon. *Phys. Chem. Chem. Phys.* **2017**, *19*, 11299–11317. [[CrossRef](#)] [[PubMed](#)]

7. Gerbaldo, M.V.; Marchetti, S.G.; Elias, V.R.; Mendieta, S.N.; Crivello, M.E. Degradation of Anti-Inflammatory Drug Diclofenac Using Cobalt Ferrite as Photocatalyst. *Chem. Eng. Res. Des.* **2021**, *166*, 237–247. [[CrossRef](#)]
8. Tabasum, A.; Alghuthaymi, M.; Qazi, U.Y.; Shahid, I.; Abbas, Q.; Javaid, R.; Nadeem, N.; Zahid, M. UV-Accelerated Photocatalytic Degradation of Pesticide over Magnetite and Cobalt Ferrite Decorated Graphene Oxide Composite. *Plants* **2020**, *10*, 6. [[CrossRef](#)]
9. Chatterjee, S.; Guha, N.; Krishnan, S.; Singh, A.K.; Mathur, P.; Rai, D.K. Selective and Recyclable Congo Red Dye Adsorption by Spherical Fe<sub>3</sub>O<sub>4</sub> Nanoparticles Functionalized with 1,2,4,5-Benzenetetracarboxylic Acid. *Sci. Rep.* **2020**, *10*, 111. [[CrossRef](#)]
10. Anantha, M.S.; Olivera, S.; Hu, C.; Jayanna, B.K.; Reddy, N.; Venkatesh, K.; Muralidhara, H.B.; Naidu, R. Comparison of the Photocatalytic, Adsorption and Electrochemical Methods for the Removal of Cationic Dyes from Aqueous Solutions. *Environ. Technol. Innov.* **2020**, *17*, 100612. [[CrossRef](#)]
11. Bilińska, L.; Gmurek, M.; Ledakowicz, S. Textile Wastewater Treatment by AOPs for Brine Reuse. *Process. Saf. Environ. Prot.* **2017**, *109*, 420–428. [[CrossRef](#)]
12. Boutra, B.; Güy, N.; Özacar, M.; Trari, M. Magnetically Separable MnFe<sub>2</sub>O<sub>4</sub>/TA/ZnO Nanocomposites for Photocatalytic Degradation of Congo Red under Visible Light. *J. Magn. Magn. Mater.* **2020**, *497*, 165994. [[CrossRef](#)]
13. Ali, T.; Tripathi, P.; Azam, A.; Raza, W.; Ahmed, A.S.; Ahmed, A.; Muneer, M. Photocatalytic Performance of Fe-Doped TiO<sub>2</sub> Nanoparticles under Visible-Light Irradiation. *Mater. Res. Express* **2017**, *4*, 015022. [[CrossRef](#)]
14. Bora, L.V.; Mewada, R.K. Visible/Solar Light Active Photocatalysts for Organic Effluent Treatment: Fundamentals, Mechanisms and Parametric Review. *Renew. Sustain. Energy Rev.* **2017**, *76*, 1393–1421. [[CrossRef](#)]
15. Fujishima, A.; Honda, K. Electrochemical Photolysis of Water at a Semiconductor Electrode. *Nature* **1972**, *238*, 37–38. [[CrossRef](#)] [[PubMed](#)]
16. Jeng, M.-J.; Wung, Y.-L.; Chang, L.-B.; Chow, L. Particle Size Effects of TiO<sub>2</sub> Layers on the Solar Efficiency of Dye-Sensitized Solar Cells. *Int. J. Photoenergy* **2013**, *2013*, 1–9. [[CrossRef](#)]
17. Thao, L.; Dang, T.; Khanitchaidecha, W.; Channei, D.; Nakaruk, A. Photocatalytic Degradation of Organic Dye under UV-A Irradiation Using TiO<sub>2</sub>-Vetiver Multifunctional Nano Particles. *Materials* **2017**, *10*, 122. [[CrossRef](#)]
18. Saliu, O.D.; Olatunji, G.A.; Yakubu, A.; Arowona, M.T.; Mohammed, A.A. Catalytic Crosslinking of a Regenerated Hydrophobic Benzylated Cellulose and Nano TiO<sub>2</sub> Composite for Enhanced Oil Absorbency. *e-Polymers* **2017**, *17*, 295–302. [[CrossRef](#)]
19. Li, H.; Zhang, T.; Pan, C.; Pu, C.; Hu, Y.; Hu, X.; Liu, E.; Fan, J. Self-Assembled Bi<sub>2</sub>MoO<sub>6</sub>/TiO<sub>2</sub> Nanofiber Heterojunction Film with Enhanced Photocatalytic Activities. *Appl. Surf. Sci.* **2017**, *391*, 303–310. [[CrossRef](#)]
20. Wang, Y.; Sunarso, J.; Zhao, B.; Ge, C.; Chen, G. One-Dimensional BiOBr Nanosheets/TiO<sub>2</sub> Nanofibers Composite: Controllable Synthesis and Enhanced Visible Photocatalytic Activity. *Ceram. Int.* **2017**, *43*, 15769–15776. [[CrossRef](#)]
21. Cheng, R.; Fan, X.; Wang, M.; Li, M.; Tian, J.; Zhang, L. Facile Construction of CuFe<sub>2</sub>O<sub>4</sub>/g-C<sub>3</sub>N<sub>4</sub> Photocatalyst for Enhanced Visible-Light Hydrogen Evolution. *RSC Adv.* **2016**, *6*, 18990–18995. [[CrossRef](#)]
22. Kefeni, K.K.; Mamba, B.B.; Msagati, T.A.M. Application of Spinel Ferrite Nanoparticles in Water and Wastewater Treatment: A Review. *Sep. Purif. Technol.* **2017**, *188*, 399–422. [[CrossRef](#)]
23. Choi, H.; Lee, S.; Kouh, T.; Kim, S.J.; Kim, C.S.; Hahn, E. Synthesis and Characterization of Co-Zn Ferrite Nanoparticles for Application to Magnetic Hyperthermia. *J. Korean Phys. Soc.* **2017**, *70*, 89–92. [[CrossRef](#)]
24. Zhang, L.; Wu, Y. Sol-Gel Synthesized Magnetic MnFe<sub>2</sub>O<sub>4</sub> Spinel Ferrite Nanoparticles as Novel Catalyst for Oxidative Degradation of Methyl Orange. *J. Nanomater.* **2013**, *2013*, 1–6. [[CrossRef](#)]
25. Waag, F.; Gökce, B.; Kalapu, C.; Bendt, G.; Salamon, S.; Landers, J.; Hagemann, U.; Heidelmann, M.; Schulz, S.; Wende, H.; et al. Adjusting the Catalytic Properties of Cobalt Ferrite Nanoparticles by Pulsed Laser Fragmentation in Water with Defined Energy Dose. *Sci. Rep.* **2017**, *7*, 13161. [[CrossRef](#)] [[PubMed](#)]
26. Qu, Q.; Zhu, A.; Shao, X.; Shi, G.; Tian, Y. Development of a Carbon Quantum Dots-Based Fluorescent Cu<sup>2+</sup> Probe Suitable for Living Cell Imaging. *Chem. Commun.* **2012**, *48*, 5473. [[CrossRef](#)]
27. Mirtchev, P.; Henderson, E.J.; Soheilnia, N.; Yip, C.M.; Ozin, G.A. Solution Phase Synthesis of Carbon Quantum Dots as Sensitizers for Nanocrystalline TiO<sub>2</sub> Solar Cells. *J. Mater. Chem.* **2012**, *22*, 1265–1269. [[CrossRef](#)]
28. Li, H.; Kang, Z.; Liu, Y.; Lee, S.-T. Carbon Nanodots: Synthesis, Properties and Applications. *J. Mater. Chem.* **2012**, *22*, 24230. [[CrossRef](#)]
29. Di, J.; Xia, J.; Ge, Y.; Li, H.; Ji, H.; Xu, H.; Zhang, Q.; Li, H.; Li, M. Novel Visible-Light-Driven CQDs/Bi<sub>2</sub>WO<sub>6</sub> Hybrid Materials with Enhanced Photocatalytic Activity toward Organic Pollutants Degradation and Mechanism Insight. *Appl. Catal. B Environ.* **2015**, *168–169*, 51–61. [[CrossRef](#)]
30. Mamba, G.; Mishra, A. Advances in Magnetically Separable Photocatalysts: Smart, Recyclable Materials for Water Pollution Mitigation. *Catalysts* **2016**, *6*, 79. [[CrossRef](#)]
31. Govan, J.; Gun'ko, Y. Recent Advances in the Application of Magnetic Nanoparticles as a Support for Homogeneous Catalysts. *Nanomaterials* **2014**, *4*, 222–241. [[CrossRef](#)]
32. Rodriguez-Arco, L.; Rodriguez, I.A.; Carriel, V.; Bonhome-Espinosa, A.B.; Campos, F.; Kuzhir, P.; Duran, J.D.G.; Lopez-Lopez, M.T. Biocompatible Magnetic Core-Shell Nanocomposites for Engineered Magnetic Tissues. *Nanoscale* **2016**, *8*, 8138–8150. [[CrossRef](#)] [[PubMed](#)]
33. Hakami, T.M.; Davarpanah, A.M.; Rahdar, A.; Barrett, S.D. Structural and Magnetic Study and Cytotoxicity Evaluation of Tetra-Metallic Nanoparticles of Co<sub>0.5</sub>Ni<sub>0.5</sub>Cr<sub>x</sub>Fe<sub>2-x</sub>O<sub>4</sub> Prepared by Co-Precipitation. *J. Mol. Struct.* **2018**, *1165*, 344–348. [[CrossRef](#)]

34. Wang, Y.; Sun, X.; Yi, Z.; Wu, X.; Liu, G.; Pu, Z.; Yang, H. Construction of a Z-Scheme  $\text{Ag}_2\text{MoO}_4/\text{BiOBr}$  Heterojunction for Photocatalytically Removing Organic Pollutants. *Dalton Trans.* **2022**, *51*, 18652–18666. [[CrossRef](#)] [[PubMed](#)]
35. Ghamkhari, A.; Mohamadi, L.; Kazemzadeh, S.; Zafar, M.N.; Rahdar, A.; Khaksefidi, R. Synthesis and Characterization of Poly(Styrene-Block-Acrylic Acid) Diblock Copolymer Modified Magnetite Nanocomposite for Efficient Removal of Penicillin G. *Compos. B: Eng.* **2020**, *182*, 107643. [[CrossRef](#)]
36. Mohammadi, L.; Rahdar, A.; Khaksefidi, R.; Ghamkhari, A.; Fytianos, G.; Kyzas, G.Z. Polystyrene Magnetic Nanocomposites as Antibiotic Adsorbents. *Polymers* **2020**, *12*, 1313. [[CrossRef](#)]
37. Ahmadi, S.; Mohammadi, L.; Rahdar, A.; Rahdar, S.; Dehghani, R.; Adaobi Igwegbe, C.; Kyzas, G.Z. Acid Dye Removal from Aqueous Solution by Using Neodymium(III) Oxide Nanoadsorbents. *Nanomaterials* **2020**, *10*, 556. [[CrossRef](#)]
38. Rahdar, S.; Rahdar, A.; Sattari, M.; Hafshejani, L.D.; Tolkou, A.K.; Kyzas, G.Z. Barium/Cobalt@Polyethylene Glycol Nanocomposites for Dye Removal from Aqueous Solutions. *Polymers* **2021**, *13*, 1161. [[CrossRef](#)]
39. Mohafez, F.S.; Davarpanah, A.M.; Rahdar, A.; Beyzaei, H.; Zeybek, O.; Barrett, S.D. Structural, Magnetic, and in Vitro Inhibitory Characteristics of Ce-Substituted  $\text{MnFe}_2\text{O}_4$  Nanoparticles. *Appl. Phys. A* **2021**, *127*, 600. [[CrossRef](#)]
40. Davarpanah, A.M.; Rahdar, A.; Dastnae, M.A.; Zeybek, O.; Beyzaei, H.  $(1-x)\text{BaFe}_{12}\text{O}_{19}/x\text{CoFe}_2\text{O}_4$  Hard/Soft Magnetic Nanocomposites: Synthesis, Physical Characterization, and Antibacterial Activities Study. *J. Mol. Struct.* **2019**, *1175*, 445–449. [[CrossRef](#)]
41. Ahmadian-Fard-Fini, S.; Salavati-Niasari, M.; Safardoust-Hojaghan, H. Hydrothermal Green Synthesis and Photocatalytic Activity of Magnetic  $\text{CoFe}_2\text{O}_4$ -Carbon Quantum Dots Nanocomposite by Turmeric Precursor. *J. Mater. Sci. Mater. Electron.* **2017**, *28*, 16205–16214. [[CrossRef](#)]
42. Kefeni, K.K.; Mamba, B.B. Photocatalytic Application of Spinel Ferrite Nanoparticles and Nanocomposites in Wastewater Treatment: Review. *Sustain. Mater. Technol.* **2020**, *23*, e00140. [[CrossRef](#)]
43. Ghasemi, A. *Magnetic Ferrites and Related Nanocomposites*, 1st ed.; Elsevier: Amsterdam, The Netherlands, 2021; p. 300.
44. Katal, R.; Masudy-Panah, S.; Tanhaei, M.; Farahani, M.H.D.A.; Jiangyong, H. A Review on the Synthesis of the Various Types of Anatase  $\text{TiO}_2$  Facets and Their Applications for Photocatalysis. *Chem. Eng. J.* **2020**, *384*, 123384. [[CrossRef](#)]
45. Kim, C.-S.; Shin, J.-W.; Cho, Y.-H.; Jang, H.-D.; Byun, H.-S.; Kim, T.-O. Synthesis and Characterization of Cu/N-Doped Mesoporous  $\text{TiO}_2$  Visible Light Photocatalysts. *Appl. Catal. A Gen.* **2013**, *455*, 211–218. [[CrossRef](#)]
46. Min, K.S.; Kumar, R.S.; Lee, J.H.; Kim, K.S.; Lee, S.G.; Son, Y.-A. Synthesis of New  $\text{TiO}_2$ /Porphyrin-Based Composites and Photocatalytic Studies on Methylene Blue Degradation. *Dyes Pigm.* **2019**, *160*, 37–47. [[CrossRef](#)]
47. Min, K.S.; Manivannan, R.; Son, Y.-A. Porphyrin Dye/ $\text{TiO}_2$  Imbedded PET to Improve Visible-Light Photocatalytic Activity and Organosilicon Attachment to Enrich Hydrophobicity to Attain an Efficient Self-Cleaning Material. *Dyes Pigm.* **2019**, *162*, 8–17. [[CrossRef](#)]
48. Wu, Q.; Zhang, Z. The Preparation of Self-Floating Sm/N Co-Doped  $\text{TiO}_2$ /Diatomite Hybrid Pellet with Enhanced Visible-Light-Responsive Photoactivity and Reusability. *Adv. Powder Technol.* **2019**, *30*, 415–422. [[CrossRef](#)]
49. Wang, G.; Ma, X.; Wei, S.; Li, S.; Qiao, J.; Wang, J.; Song, Y. Highly Efficient Visible-Light Driven Photocatalytic Hydrogen Production from a Novel Z-Scheme  $\text{Er}^{3+}:\text{YAlO}_3/\text{Ta}_2\text{O}_5\text{-V}^{5+} \parallel \text{Fe}^{3+}\text{-TiO}_2/\text{Au}$  Coated Composite. *J. Power Sources* **2018**, *373*, 161–171. [[CrossRef](#)]
50. Lee, H.U.; Lee, S.C.; Choi, S.; Son, B.; Lee, S.M.; Kim, H.J.; Lee, J. Efficient Visible-Light Induced Photocatalysis on Nanoporous Nitrogen-Doped Titanium Dioxide Catalysts. *Chem. Eng. J.* **2013**, *228*, 756–764. [[CrossRef](#)]
51. Krasil'nikov, V.N.; Shalaeva, E.V.; Baklanova, I.V.; Melkozerova, M.A.; Kuznetsov, M.V.; Zabolotskaya, E.V.; Gyrdasova, O.I.; Buldakova, L.Y.; Murzakaev, A.M. Synthesis, Structure and Spectroscopic Characteristics of  $\text{Ti}(\text{O,C})_2$ /Carbon Nanostructured Globules with Visible Light Photocatalytic Activity. *Bull. Mater. Sci.* **2016**, *39*, 1569–1579. [[CrossRef](#)]
52. Ju, T.; Lee, H.; Kang, M. The Photovoltaic Efficiency of Dye Sensitized Solar Cell Assembled Using Carbon Capsulated  $\text{TiO}_2$  Electrode. *J. Ind. Eng. Chem.* **2014**, *20*, 2636–2640. [[CrossRef](#)]
53. Chen, P.; Wang, F.; Chen, Z.-F.; Zhang, Q.; Su, Y.; Shen, L.; Yao, K.; Liu, Y.; Cai, Z.; Lv, W.; et al. Study on the Photocatalytic Mechanism and Detoxicity of Gemfibrozil by a Sunlight-Driven  $\text{TiO}_2$ /Carbon Dots Photocatalyst: The Significant Roles of Reactive Oxygen Species. *Appl. Catal. B Environ.* **2017**, *204*, 250–259. [[CrossRef](#)]
54. Surenjan, A.; Sambandam, B.; Pradeep, T.; Philip, L. Synthesis, Characterization and Performance of Visible Light Active C- $\text{TiO}_2$  for Pharmaceutical Photodegradation. *J. Environ. Chem. Eng.* **2017**, *5*, 757–767. [[CrossRef](#)]
55. Li, X.-W.; Yuan, Y.; Huang, X.; Lin, K.-F. Visible-Infrared Optical Properties Measurement of the Mesoporous  $\text{TiO}_2$ /Carbon Materials. *Int. J. Hydrog. Energy* **2016**, *41*, 15638–15645. [[CrossRef](#)]
56. Wanag, A.; Kusiak-Nejman, E.; Kapica-Kozar, J.; Morawski, A.W. Photocatalytic Performance of Thermally Prepared  $\text{TiO}_2$ /C Photocatalysts under Artificial Solar Light. *Micro Nano Lett.* **2016**, *11*, 202–206. [[CrossRef](#)]
57. Neville, E.M.; Ziegler, J.; Don MacElroy, J.M.; Ravindranathan Thampi, K.; Sullivan, J.A. Serendipity Following Attempts to Prepare C-Doped Rutile  $\text{TiO}_2$ . *Appl. Catal. A Gen.* **2014**, *470*, 434–441. [[CrossRef](#)]
58. Teh, C.Y.; Wu, T.Y.; Juan, J.C. An Application of Ultrasound Technology in Synthesis of Titania-Based Photocatalyst for Degrading Pollutant. *Chem. Eng. J.* **2017**, *317*, 586–612. [[CrossRef](#)]
59. Reli, M.; Kobielski, M.; Matějová, L.; Daniš, S.; Macyk, W.; Obalová, L.; Kuštrowski, P.; Rokicińska, A.; Kočí, K.  $\text{TiO}_2$  Processed by Pressurized Hot Solvents as a Novel Photocatalyst for Photocatalytic Reduction of Carbon Dioxide. *Appl. Surf. Sci.* **2017**, *391*, 282–287. [[CrossRef](#)]

60. Rahimi, N.; Pax, R.A.; Gray, E.; Mac, A. Review of Functional Titanium Oxides. I: TiO<sub>2</sub> and Its Modifications. *Prog. Solid State Chem.* **2016**, *44*, 86–105. [CrossRef]
61. Mikrut, P.; Kobielski, M.; Macyk, W. Spectroelectrochemical Characterization of Euhedral Anatase TiO<sub>2</sub> Crystals—Implications for Photoelectrochemical and Photocatalytic Properties of {001} {100} and {101} Facets. *Electrochim. Acta* **2019**, *310*, 256–265. [CrossRef]
62. Surówka, M.; Kobielski, M.; Trochowski, M.; Buchalska, M.; Kruczała, K.; Broś, P.; Macyk, W. Iron and Other Metal Species as Phase-Composition Controllers Influencing the Photocatalytic Activity of TiO<sub>2</sub> Materials. *Appl. Catal. B Environ.* **2019**, *247*, 173–181. [CrossRef]
63. Sadowski, R.; Wach, A.; Buchalska, M.; Kuśtrowski, P.; Macyk, W. Photosensitized TiO<sub>2</sub> Films on Polymers—Titania-Polymer Interactions and Visible Light Induced Photoactivity. *Appl. Surf. Sci.* **2019**, *475*, 710–719. [CrossRef]
64. Karthik, K.; Vijayalakshmi, S.; Phuruangrat, A.; Revathi, V.; Verma, U. Multifunctional Applications of Microwave-Assisted Biogenic TiO<sub>2</sub> Nanoparticles. *J. Clust. Sci.* **2019**, *30*, 965–972. [CrossRef]
65. Mahdavi-Shakib, A.; Husremovic, S.; Ki, S.; Glynn, J.; Babb, L.; Sempel, J.; Stavrinoudis, I.; Arce-Ramos, J.-M.; Nelson, R.; Grabow, L.C.; et al. Titania Surface Chemistry and Its Influence on Supported Metal Catalysts. *Polyhedron* **2019**, *170*, 41–50. [CrossRef]
66. Fatima, R.; Afridi, M.N.; Kumar, V.; Lee, J.; Ali, I.; Kim, K.-H.; Kim, J.-O. Photocatalytic Degradation Performance of Various Types of Modified TiO<sub>2</sub> against Nitrophenols in Aqueous Systems. *J. Clean. Prod.* **2019**, *231*, 899–912. [CrossRef]
67. Boro, B.; Gogoi, B.; Rajbongshi, B.M.; Ramchiary, A. Nano-Structured TiO<sub>2</sub>/ZnO Nanocomposite for Dye-Sensitized Solar Cells Application: A Review. *Renew. Sustain. Energy Rev.* **2018**, *81*, 2264–2270. [CrossRef]
68. Akhter, P.; Farkhondehfar, M.A.; Hernández, S.; Hussain, M.; Fina, A.; Saracco, G.; Khan, A.U.; Russo, N. Environmental Issues Regarding CO<sub>2</sub> and Recent Strategies for Alternative Fuels through Photocatalytic Reduction with Titania-Based Materials. *J. Environ. Chem. Eng.* **2016**, *4*, 3934–3953. [CrossRef]
69. Ashraf, S.; Siddiq, A.; Shahida, S.; Qaisar, S. Titanium-Based Nanocomposite Materials for Arsenic Removal from Water: A Review. *Heliyon* **2019**, *5*, e01577. [CrossRef]
70. Etacheri, V.; Michlits, G.; Seery, M.K.; Hinder, S.J.; Pillai, S.C. A Highly Efficient TiO<sub>2-x</sub>C<sub>x</sub> Nano-Heterojunction Photocatalyst for Visible Light Induced Antibacterial Applications. *ACS Appl. Mater. Interfaces* **2013**, *5*, 1663–1672. [CrossRef]
71. Di Valentin, C.; Pacchioni, G. Trends in Non-Metal Doping of Anatase TiO<sub>2</sub>: B, C, N and F. *Catal. Today* **2013**, *206*, 12–18. [CrossRef]
72. Tatarchuk, T.; Mironyuk, I.; Kotsyubynsky, V.; Shyichuk, A.; Myslin, M.; Boychuk, V. Structure, Morphology and Adsorption Properties of Titania Shell Immobilized onto Cobalt Ferrite Nanoparticle Core. *J. Mol. Liq.* **2020**, *297*, 111757. [CrossRef]
73. Dadfar, M.R.; Seyyed Ebrahimi, S.A.; Masoudpanah, S.M. Sol-Gel Synthesis and Characterization of SrFe<sub>12</sub>O<sub>19</sub>/TiO<sub>2</sub> Nanocomposites. *J. Supercond. Nov. Magn.* **2015**, *28*, 89–94. [CrossRef]
74. Xu, S.; Feng, D.; Shangguan, W. Preparations and Photocatalytic Properties of Visible-Light-Active Zinc Ferrite-Doped TiO<sub>2</sub> Photocatalyst. *J. Phys. Chem. C* **2009**, *113*, 2463–2467. [CrossRef]
75. Lahijani, B.; Hedayati, K.; Goodarzi, M. Magnetic PbFe<sub>12</sub>O<sub>19</sub>-TiO<sub>2</sub> Nanocomposites and Their Photocatalytic Performance in the Removal of Toxic Pollutants. *Main Group Met. Chem.* **2018**, *41*, 53–62. [CrossRef]
76. De Lucena, P.R.; Pessoa-Neto, O.D.; Dos Santos, I.M.G.; Souza, A.G.; Longo, E.; Varela, J.A. Synthesis by the Polymeric Precursor Method and Characterization of Undoped and Sn, Cr and V-Doped ZrTiO. *J. Alloys Compd.* **2005**, *397*, 255–259. [CrossRef]
77. Mourão, H.A.J.L.; Malagutti, A.R.; Ribeiro, C. Synthesis of TiO<sub>2</sub>-Coated CoFe<sub>2</sub>O<sub>4</sub> Photocatalysts Applied to the Photodegradation of Atrazine and Rhodamine B in Water. *Appl. Catal. A Gen.* **2010**, *382*, 284–292. [CrossRef]
78. Mohanty, P.; Mahapatra, R.; Padhi, P.; Ramana, C.V.V.; Mishra, D.K. Ultrasonic Cavitation: An Approach to Synthesize Uniformly Dispersed Metal Matrix Nanocomposites—A Review. *Nano Struct. Nano Objects* **2020**, *23*, 100475. [CrossRef]
79. Ley, S.V.; Low, C.M.R. *Ultrasound in Synthesis*; Springer: Berlin/Heidelberg, Germany, 1989; p. 133.
80. Ao, Y.; Xu, J.; Fu, D.; Shen, X.; Yuan, C. A Novel Magnetically Separable Composite Photocatalyst: Titania-Coated Magnetic Activated Carbon. *Sep. Purif. Technol.* **2008**, *61*, 436–441. [CrossRef]
81. Jiang, W.; Zhang, X.; Gong, X.; Yan, F.; Zhang, Z. Sonochemical Synthesis and Characterization of Magnetic Separable Fe<sub>3</sub>O<sub>4</sub>-TiO<sub>2</sub> Nanocomposites and Their Catalytic Properties. *Int. J. Smart Nano Mater.* **2010**, *1*, 278–287. [CrossRef]
82. Rane, A.V.; Kanny, K.; Abitha, V.K.; Thomas, S. *Synthesis of Inorganic Nanomaterials*; Bhagyaraj, S.M., Oluwafemi, O.S., Kalarikkal, N., Thomas, S., Eds.; Elsevier: Amsterdam, The Netherlands, 2018; pp. 121–139.
83. Sathishkumar, P.; Mangalaraja, R.V.; Anandan, S.; Ashokkumar, M. CoFe<sub>2</sub>O<sub>4</sub>/TiO<sub>2</sub> Nanocatalysts for the Photocatalytic Degradation of Reactive Red 120 in Aqueous Solutions in the Presence and Absence of Electron Acceptors. *Chem. Eng. J.* **2013**, *220*, 302–310. [CrossRef]
84. Chandrika, M.; Ravindra, A.V.; Rajesh, C.; Ramarao, S.D.; Ju, S. Studies on Structural and Optical Properties of Nano ZnFe<sub>2</sub>O<sub>4</sub> and ZnFe<sub>2</sub>O<sub>4</sub>-TiO<sub>2</sub> Composite Synthesized by Co-Precipitation Route. *Mater. Chem. Phys.* **2019**, *230*, 107–113. [CrossRef]
85. Haw, C.; Chiu, W.; Abdul Rahman, S.; Khiew, P.; Radiman, S.; Abdul Shukor, R.; Hamid, M.A.A.; Ghazali, N. The Design of New Magnetic-Photocatalyst Nanocomposites (CoFe<sub>2</sub>O<sub>4</sub>-TiO<sub>2</sub>) as Smart Nanomaterials for Recyclable-Photocatalysis Applications. *New J. Chem.* **2016**, *40*, 1124–1136. [CrossRef]
86. Allaedini, G.; Tasirin, S.M.; Aminayi, P. Magnetic Properties of Cobalt Ferrite Synthesized by Hydrothermal Method. *Int. Nano Lett.* **2015**, *5*, 183–186. [CrossRef]

87. Aziz, A.A.; Puma, G.L.; Ibrahim, S.; Saravanan, P. Preparation, Characterisation and Solar Photoactivity of Titania Supported Strontium Ferrite Nanocomposite Photocatalyst. *J. Exp. Nanosci.* **2013**, *8*, 295–310. [[CrossRef](#)]
88. Nguyen, T.B.; Doong, R. Fabrication of Highly Visible-Light-Responsive ZnFe<sub>2</sub>O<sub>4</sub>/TiO<sub>2</sub> Heterostructures for the Enhanced Photocatalytic Degradation of Organic Dyes. *RSC Adv.* **2016**, *6*, 103428–103437. [[CrossRef](#)]
89. Pongwan, P.; Inceesungvorn, B.; Phanichphant, S.; Kangwansupamonkon, W.; Wetchakun, N. Synthesis and Characterization of a Magnetically Separable CoFe<sub>2</sub>O<sub>4</sub>/TiO<sub>2</sub> Nanocomposite for the Photomineralization of Formic Acid. *Ferroelectrics* **2013**, *453*, 133–140. [[CrossRef](#)]
90. Sun, J.; Fu, Y.; Xiong, P.; Sun, X.; Xu, B.; Wang, X. A Magnetically Separable P25/CoFe<sub>2</sub>O<sub>4</sub>/Graphene Catalyst with Enhanced Adsorption Capacity and Visible-Light-Driven Photocatalytic Activity. *RSC Adv.* **2013**, *3*, 22490. [[CrossRef](#)]
91. Etacheri, V.; Di Valentin, C.; Schneider, J.; Bahnemann, D.; Pillai, S.C. Visible-Light Activation of TiO<sub>2</sub> Photocatalysts: Advances in Theory and Experiments. *J. Photochem. Photobiol. C Photochem. Rev.* **2015**, *25*, 1–29. [[CrossRef](#)]
92. Atacan, K.; Güy, N.; Çakar, S. Preparation and Antibacterial Activity of Solvothermal Synthesized ZnFe<sub>2</sub>O<sub>4</sub>/Ag-TiO<sub>2</sub> Nanocomposite. *Sakarya Uni. J. Sci.* **2018**, *22*, 1720–1726. [[CrossRef](#)]
93. Nguyen, T.B.; Doong, R. Heterostructured ZnFe<sub>2</sub>O<sub>4</sub>/TiO<sub>2</sub> Nanocomposites with a Highly Recyclable Visible-Light-Response for Bisphenol A Degradation. *RSC Adv.* **2017**, *7*, 50006–50016. [[CrossRef](#)]
94. Deng, Y.-H.; Wang, C.-C.; Hu, J.-H.; Yang, W.-L.; Fu, S.-K. Investigation of Formation of Silica-Coated Magnetite Nanoparticles via Sol–Gel Approach. *Colloids Surf. A Physicochem. Eng. Asp.* **2005**, *262*, 87–93. [[CrossRef](#)]
95. Sounderya, N.; Zhang, Y. Use of Core/Shell Structured Nanoparticles for Biomedical Applications. *Biomedical* **2008**, *1*, 34–42. [[CrossRef](#)]
96. Morales, A.E.; Mora, E.S.; Pal, U. Use of diffuse reflectance spectroscopy for optical characterization of unsupported nanostructures. *Rev. Mex. Fis.* **2007**, *53*, 18–22.
97. Bardapurkar, P.P.; Shewale, S.S.; Barde, N.P.; Jadhav, K.M. Structural, Magnetic and Catalytical Properties of Cobalt Ferrite Nanoparticles Dispersed in Silica Matrix. *Mater. Res. Express.* **2019**, *6*, 045055. [[CrossRef](#)]
98. Gharagozlou, M. Influence of Calcination Temperature on Structural and Magnetic Properties of Nanocomposites Formed by Co-Ferrite Dispersed in Sol-Gel Silica Matrix Using Tetrakis(2-Hydroxyethyl) Orthosilicate as Precursor. *Chem. Cent. J.* **2011**, *5*, 19. [[CrossRef](#)] [[PubMed](#)]
99. Pansambal, S.; Ghotekar, S.; Shewale, S.; Deshmukh, K.; Barde, N.; Bardapurkar, P. Efficient Synthesis of Magnetically Separable CoFe<sub>2</sub>O<sub>4</sub>@SiO<sub>2</sub> Nanoparticles and Its Potent Catalytic Applications for the Synthesis of 5-Aryl-1,2,4-Triazolidine-3-Thione Derivatives. *J. Water Environ. Nanotechnol.* **2019**, *4*, 174–186. [[CrossRef](#)]
100. Dippong, T.; Levei, E.A.; Cadar, O. Preparation of CoFe<sub>2</sub>O<sub>4</sub>/SiO<sub>2</sub> Nanocomposites at Low Temperatures Using Short Chain Diols. *J. Chem.* **2017**, *2017*, 1–11. [[CrossRef](#)]
101. Stöber, W.; Fink, A.; Bohn, E. Controlled Growth of Monodisperse Silica Spheres in the Micron Size Range. *J. Colloid Interface Sci.* **1968**, *26*, 62–69. [[CrossRef](#)]
102. Ehi-Eromosele, C.O.; Ita, B.I.; Iweala, E.E.J.; Ogunniran, K.O.; Adekoya, J.A.; Siyanbola, T.O. Silica Functionalized Magnesium Ferrite Nanocomposites for Potential Biomedical Applications: Preparation, Characterization and Enhanced Colloidal Stability Studies. *J. Nano Res.* **2016**, *40*, 146–157. [[CrossRef](#)]
103. Khanna, L.; Verma, N.K. Silica/Potassium Ferrite Nanocomposite: Structural, Morphological, Magnetic, Thermal and in Vitro Cytotoxicity Analysis. *Mater. Eng. B* **2013**, *178*, 1230–1239. [[CrossRef](#)]
104. Flood-Garibay, J.A.; Méndez-Rojas, M.A. Synthesis and Characterization of Magnetic Nanoparticles of Cobalt Ferrite Coated with Silica. *Biointerface Res. Appl. Chem.* **2019**, *10*, 4908–4913. [[CrossRef](#)]
105. Girgis, E.; Wahsh, M.M.; Othman, A.G.; Bandhu, L.; Rao, K. Synthesis, Magnetic and Optical Properties of Core/Shell Co<sub>1-x</sub>Zn<sub>x</sub>Fe<sub>2</sub>O<sub>4</sub>/SiO<sub>2</sub> Nanoparticles. *Nanoscale Res. Lett.* **2011**, *6*, 460. [[CrossRef](#)] [[PubMed](#)]
106. Rohilla, S.; Kumar, S.; Aghamkar, P.; Sunder, S.; Agarwal, A. Investigations on Structural and Magnetic Properties of Cobalt Ferrite/Silica Nanocomposites Prepared by the Coprecipitation Method. *J. Magn. Magn. Mater.* **2011**, *323*, 897–902. [[CrossRef](#)]
107. Bansal, M.; Ahlawat, D.S.; Singh, A.; Kumar, V.; Rathee, S.P. Effect of Heat Treatment on the Microstructural Properties of Silica Embedded Cobalt Ferrite Nanocomposites. *Nanocomposites* **2020**, *6*, 158–164. [[CrossRef](#)]
108. Yakob, M.; Umar, H.; Wahyuningsih, P.; Putra, R.A. Characterization of microstructural and optical CoFe<sub>2</sub>O<sub>4</sub>/SiO<sub>2</sub> ferrite nanocomposite for photodegradation of methylene blue. *AIMS Mater. Sci.* **2019**, *6*, 45–51. [[CrossRef](#)]
109. Sharma, S.; Rohilla, S. Synthesis of Nanocomposites of NiFe<sub>2</sub>O<sub>4</sub>/SiO<sub>2</sub> through Coprecipitation Method and Structural Characterization Using Rietveld Refinement. In Proceedings of the AIP Conference Proceedings, Seoul, Republic of Korea, 2 November 2020; p. 110023.
110. Kong, L.B.; Zhang, T.S.; Ma, J.; Boey, F. Progress in Synthesis of Ferroelectric Ceramic Materials via High-Energy Mechanochemical Technique. *Prog. Mater. Sci.* **2008**, *53*, 207–322. [[CrossRef](#)]
111. Aguilar-González, M.A.; Mendoza-Suárez, G.; Padmasree, K.P. Synthesis and Characterization of Barium Ferrite–Silica Nanocomposites. *Mater. Charact.* **2013**, *84*, 175–181. [[CrossRef](#)]
112. Scano, A.; Cabras, V.; Marongiu, F.; Peddis, D.; Pilloni, M.; Ennas, G. New Opportunities in the Preparation of Nanocomposites for Biomedical Applications: Revised Mechanochemical Synthesis of Magnetite–Silica Nanocomposites. *Mater. Res. Express* **2017**, *4*, 025004. [[CrossRef](#)]

113. Xu, Y.; Tang, C.-J.; Huang, H.; Sun, C.-Q.; Zhang, Y.-K.; Ye, Q.-F.; Wang, A.-J. Green Synthesis of Fluorescent Carbon Quantum Dots for Detection of Hg<sup>2+</sup>. *Chin. J. Anal. Chem.* **2014**, *42*, 1252–1258. [[CrossRef](#)]
114. De, B.; Karak, N. A Green and Facile Approach for the Synthesis of Water Soluble Fluorescent Carbon Dots from Banana Juice. *RSC Adv.* **2013**, *3*, 8286. [[CrossRef](#)]
115. Gao, Z.; Wang, X.; Chang, J.; Wu, D.; Wang, L.; Liu, X.; Xu, F.; Guo, Y.; Jiang, K. Fluorescent Carbon Quantum Dots, Capacitance and Catalysis Active Porous Carbon Microspheres from Beer. *RSC Adv.* **2015**, *5*, 48665–48674. [[CrossRef](#)]
116. Wee, S.S.; Ng, Y.H.; Ng, S.M. Synthesis of Fluorescent Carbon Dots via Simple Acid Hydrolysis of Bovine Serum Albumin and Its Potential as Sensitive Sensing Probe for Lead (II) Ions. *Talanta* **2013**, *116*, 71–76. [[CrossRef](#)] [[PubMed](#)]
117. Wang, Q.; Zhang, C.; Shen, G.; Liu, H.; Fu, H.; Cui, D. Fluorescent Carbon Dots as an Efficient siRNA Nanocarrier for Its Interference Therapy in Gastric Cancer Cells. *J. Nanobiotechnol.* **2014**, *12*, 58. [[CrossRef](#)] [[PubMed](#)]
118. Vitha, T.S. Quantitative Evaluation of Pytochemicals from Terminalia Chebula by High Performance Thin Layer Chromatography (HPTLC) Method and Its Antibiofilm Activity. *Int. J. Pharma Bio Sci.* **2017**, *8*, 214–224. [[CrossRef](#)]
119. Moradi, B.; Nabiyouni, G.; Ghanbari, D. Rapid Photo-Degradation of Toxic Dye Pollutants: Green Synthesis of Mono-Disperse Fe<sub>3</sub>O<sub>4</sub>-CeO<sub>2</sub> Nanocomposites in the Presence of Lemon Extract. *J. Mater. Sci. Mater. Electron.* **2018**, *29*, 11065–11080. [[CrossRef](#)]
120. Barman, M.K.; Patra, A. Current Status and Prospects on Chemical Structure Driven Photoluminescence Behaviour of Carbon Dots. *J. Photochem. Photobiol. C* **2018**, *37*, 1–22. [[CrossRef](#)]
121. Das, R.; Bandyopadhyay, R.; Pramanik, P. Carbon Quantum Dots from Natural Resource: A Review. *Mater. Today Chem.* **2018**, *8*, 96–109. [[CrossRef](#)]
122. Ahmadian-Fard-Fini, S.; Salavati-Niasari, M.; Ghanbari, D. Hydrothermal Green Synthesis of Magnetic Fe<sub>3</sub>O<sub>4</sub>-Carbon Dots by Lemon and Grape Fruit Extracts and as a Photoluminescence Sensor for Detecting of *E. Coli* Bacteria. *Spectrochim. Acta Mol. Biomol. Spectrosc.* **2018**, *203*, 481–493. [[CrossRef](#)]
123. Baragau, I.-A.; Power, N.P.; Morgan, D.J.; Heil, T.; Lobo, R.A.; Roberts, C.S.; Titirici, M.-M.; Dunn, S.; Kellici, S. Continuous Hydrothermal Flow Synthesis of Blue-Luminescent, Excitation-Independent Nitrogen-Doped Carbon Quantum Dots as Nanosensors. *J. Mater. Chem. A* **2020**, *8*, 3270–3279. [[CrossRef](#)]
124. Wang, Y.; Hu, A. Carbon Quantum Dots: Synthesis, Properties and Applications. *J. Mater. Chem. C* **2014**, *2*, 6921. [[CrossRef](#)]
125. Liu, J.-H.; Cao, L.; LeCroy, G.E.; Wang, P.; Meziani, M.J.; Dong, Y.; Liu, Y.; Luo, P.G.; Sun, Y.-P. Carbon “Quantum” Dots for Fluorescence Labeling of Cells. *ACS Appl. Mater. Interfaces* **2015**, *7*, 19439–19445. [[CrossRef](#)]
126. Dong, X.; Liang, W.; Meziani, M.J.; Sun, Y.-P.; Yang, L. Carbon Dots as Potent Antimicrobial Agents. *Theranostics* **2020**, *10*, 671–686. [[CrossRef](#)]
127. Ahmadian-Fard-Fini, S.; Ghanbari, D.; Salavati-Niasari, M. Photoluminescence Carbon Dot as a Sensor for Detecting of *Pseudomonas Aeruginosa* Bacteria: Hydrothermal Synthesis of Magnetic Hollow NiFe<sub>2</sub>O<sub>4</sub>-Carbon Dots Nanocomposite Material. *Compos. Part B Eng.* **2019**, *161*, 564–577. [[CrossRef](#)]
128. Huang, Y.; Liang, Y.; Rao, Y.; Zhu, D.; Cao, J.; Shen, Z.; Ho, W.; Lee, S.C. Environment-Friendly Carbon Quantum Dots/ZnFe<sub>2</sub>O<sub>4</sub> Photocatalysts: Characterization, Biocompatibility, and Mechanisms for NO Removal. *Environ. Sci. Technol.* **2017**, *51*, 2924–2933. [[CrossRef](#)] [[PubMed](#)]
129. Chen, C.C.; Fan, T. Study on Carbon Quantum Dots/BiFeO<sub>3</sub> Heterostructures and Their Enhanced Photocatalytic Activities under Visible Light Irradiation. *J. Mater. Sci. Mater. Electron.* **2017**, *28*, 10019–10027. [[CrossRef](#)]
130. Nabiyouni, G.; Ghanbari, D. Hydrothermal Synthesis of Magnetic and Photoluminescence CuFe<sub>2</sub>O<sub>4</sub>-Carbon Dots Nanocomposite as a Sensor for Detecting of Hg<sup>II</sup> Ions. *J. Nanostruct.* **2020**, *10*, 760–768. [[CrossRef](#)]
131. Rahman, I.A.; Padavettan, V. Synthesis of Silica Nanoparticles by Sol-Gel: Size-Dependent Properties, Surface Modification, and Applications in Silica-Polymer Nanocomposites—A Review. *J. Nanomater.* **2012**, *2012*, 1–15. [[CrossRef](#)]
132. Hagens, W.I.; Oomen, A.G.; De Jong, W.H.; Cassee, F.R.; Sips, A.J.A.M. What Do We (Need to) Know about the Kinetic Properties of Nanoparticles in the Body? *J. Regul. Toxicol. Pharmacol.* **2007**, *49*, 217–229. [[CrossRef](#)]
133. Mathiazhagan, A.; Joseph, R. Nanotechnology—A New Prospective in Organic Coating-Review. *Int. J. Chem. Eng. Appl.* **2011**, *2*, 225–237. [[CrossRef](#)]
134. Nalathambi, V.; Suresh, G. Contribution of Nanotechnology in The Paints and Coatings. *Int. J. Chem. Eng. Res.* **2014**, *1*, 116–186. [[CrossRef](#)]
135. Singh, R.; Thirupathi, G. *Manganese-Zinc Spinel Ferrite Nanoparticles and Ferrofluids*; Singh, R., Thirupathied, G., Eds.; InTech: London, UK, 2017; pp. 140–159.
136. Peng, Y.; Wang, Z.; Liu, W.; Zhang, H.; Zuo, W.; Tang, H.; Chen, F.; Wang, B. Size-and Shape-Dependent Peroxidase-like Catalytic Activity of MnFe<sub>2</sub>O<sub>4</sub> Nanoparticles and Their Applications in Highly Efficient Colorimetric Detection of Target Cancer Cells. *Dalton Trans.* **2015**, *44*, 12871–12877. [[CrossRef](#)]
137. Reddy, S.; Kumara Swamy, B.E.; Chandra, U.; Mahathesha, K.R.; Sathisha, T.V.; Jayadevappa, H. Synthesis of MgFe<sub>2</sub>O<sub>4</sub> Nanoparticles and MgFe<sub>2</sub>O<sub>4</sub> Nanoparticles/CPE for Electrochemical Investigation of Dopamine. *Anal. Methods* **2011**, *3*, 2792. [[CrossRef](#)]
138. Céspedes, E.; Byrne, J.M.; Farrow, N.; Moise, S.; Coker, V.S.; Bencsik, M.; Lloyd, J.R.; Telling, N.D. Bacterially Synthesized Ferrite Nanoparticles for Magnetic Hyperthermia Applications. *Nanoscale* **2014**, *6*, 12958–12970. [[CrossRef](#)] [[PubMed](#)]
139. Pardeshi, S.K.; Pawar, R.Y. SrFe<sub>2</sub>O<sub>4</sub> Complex Oxide an Effective and Environmentally Benign Catalyst for Selective Oxidation of Styrene. *J. Mol. Catal. A Chem.* **2011**, *334*, 35–43. [[CrossRef](#)]

140. Khedr, M.H.; Abdel Halim, K.S.; Soliman, N.K. Synthesis and Photocatalytic Activity of Nano-Sized Iron Oxides. *Mater. Lett.* **2009**, *63*, 598–601. [[CrossRef](#)]
141. Surendra, B.S. Green Engineered Synthesis of Ag-Doped  $\text{CuFe}_2\text{O}_4$ : Characterization, Cyclic Voltammetry and Photocatalytic Studies. *J. Sci. Adv. Mater. Dev.* **2018**, *3*, 44–50. [[CrossRef](#)]
142. Diao, Y.; Yan, Z.; Guo, M.; Wang, X. Magnetic Multi-Metal Co-Doped Magnesium Ferrite Nanoparticles: An Efficient Visible Light-Assisted Heterogeneous Fenton-like Catalyst Synthesized from Saproliite Laterite Ore. *J. Hazard. Mater.* **2018**, *344*, 829–838. [[CrossRef](#)]
143. Han, X.; Zhang, H.; Chen, T.; Zhang, M.; Guo, M. Facile Synthesis of Metal-Doped Magnesium Ferrite from Saproliite Laterite as an Effective Heterogeneous Fenton-like Catalyst. *J. Mol. Liq.* **2018**, *272*, 43–52. [[CrossRef](#)]
144. Feng, Y.; Liao, C.; Shih, K. Copper-Promoted Circumneutral Activation of  $\text{H}_2\text{O}_2$  by Magnetic  $\text{CuFe}_2\text{O}_4$  Spinel Nanoparticles: Mechanism, Stoichiometric Efficiency, and Pathway of Degrading Sulfanilamide. *Chemosphere* **2016**, *154*, 573–582. [[CrossRef](#)]
145. Wang, G.; Zhao, D.; Kou, F.; Ouyang, Q.; Chen, J.; Fang, Z. Removal of Norfloxacin by Surface Fenton System ( $\text{MnFe}_2\text{O}_4/\text{H}_2\text{O}_2$ ): Kinetics, Mechanism and Degradation Pathway. *Chem. Eng. J.* **2018**, *351*, 747–755. [[CrossRef](#)]
146. Guo, X.; Wang, D. Photo-Fenton Degradation of Methylene Blue by Synergistic Action of Oxalic Acid and Hydrogen Peroxide with  $\text{NiFe}_2\text{O}_4$  Hollow Nanospheres Catalyst. *J. Environ. Chem. Eng.* **2019**, *7*, 102814. [[CrossRef](#)]
147. Moreno-Castilla, C.; López-Ramón, M.V.; Fontecha-Cámara, M.Á.; Álvarez, M.A.; Mateus, L. Removal of Phenolic Compounds from Water Using Copper Ferrite Nanosphere Composites as Fenton Catalysts. *Nanomaterials* **2019**, *9*, 901. [[CrossRef](#)] [[PubMed](#)]
148. Yao, H.; Fan, M.; Wang, Y.; Luo, G.; Fei, W. Magnetic Titanium Dioxide Based Nanomaterials: Synthesis, Characteristics, and Photocatalytic Application in Pollutant Degradation. *J. Mater. Chem. A* **2015**, *3*, 17511–17524. [[CrossRef](#)]
149. Schneider, J.; Matsuoka, M.; Takeuchi, M.; Zhang, J.; Horiuchi, Y.; Anpo, M.; Bahnemann, D.W. Understanding  $\text{TiO}_2$  Photocatalysis: Mechanisms and Materials. *Chem. Rev.* **2014**, *114*, 9919–9986. [[CrossRef](#)] [[PubMed](#)]
150. Yeganeh, M.; Shahtahmasebi, N.; Kompany, A.; Karimipour, M.; Razavi, F.; Nasralla, N.H.S.; Šiller, L. The Magnetic Characterization of Fe Doped  $\text{TiO}_2$  Semiconducting Oxide Nanoparticles Synthesized by Sol–Gel Method. *Physical. B Condens. Matter* **2017**, *511*, 89–98. [[CrossRef](#)]
151. Lin, Z.; Xu, Y.; Zhen, Z.; Fu, Y.; Liu, Y.; Li, W.; Luo, C.; Ding, A.; Zhang, D. Application and Reactivation of Magnetic Nanoparticles in *Microcystis Aeruginosa* Harvesting. *Bioresour. Technol.* **2015**, *190*, 82–88. [[CrossRef](#)]
152. Wang, X.; Zhao, X.; Li, H.; Jia, J.; Liu, Y.; Ejenavi, O.; Ding, A.; Sun, Y.; Zhang, D. Separating and Characterizing Functional Alkane Degradation from Crude-Oil-Contaminated Sites via Magnetic Nanoparticle-Mediated Isolation. *Res. Microbiol.* **2016**, *167*, 731–744. [[CrossRef](#)]
153. Zhang, P.; Mo, Z.; Han, L.; Zhu, X.; Wang, B.; Zhang, C. Preparation and Photocatalytic Performance of Magnetic  $\text{TiO}_2/\text{Montmorillonite}/\text{Fe}_3\text{O}_4$  Nanocomposites. *Ind. Eng. Chem. Res.* **2014**, *53*, 8057–8061. [[CrossRef](#)]
154. Chen, Z.; Ma, Y.; Geng, B.; Wang, M.; Sun, X. Photocatalytic Performance and Magnetic Separation of  $\text{TiO}_2$ -Functionalized  $\gamma\text{-Fe}_2\text{O}_3$ , Fe, and Fe/ $\text{Fe}_2\text{O}_3$  Magnetic Particles. *J. Alloys Compd.* **2017**, *700*, 113–121. [[CrossRef](#)]
155. Chen, C.-C.; Jaihindh, D.; Hu, S.-H.; Fu, Y.-P. Magnetic Recyclable Photocatalysts of Ni-Cu-Zn Ferrite@ $\text{SiO}_2$ @ $\text{TiO}_2$ @Ag and Their Photocatalytic Activities. *J. Photochem. Photobiol. A Chem.* **2017**, *334*, 74–85. [[CrossRef](#)]
156. Moreira, F.C.; Boaventura, R.A.R.; Brillas, E.; Vilar, V.J.P. Electrochemical Advanced Oxidation Processes: A Review on Their Application to Synthetic and Real Wastewaters. *Appl. Catal. B Environ.* **2017**, *202*, 217–261. [[CrossRef](#)]
157. Boczkaj, G.; Fernandes, A. Wastewater Treatment by Means of Advanced Oxidation Processes at Basic pH Conditions: A Review. *Chem. Eng. J.* **2017**, *320*, 608–633. [[CrossRef](#)]
158. Dewil, R.; Mantzavinos, D.; Poullos, I.; Rodrigo, M.A. New Perspectives for Advanced Oxidation Processes. *J. Environ. Manag.* **2017**, *195*, 93–99. [[CrossRef](#)] [[PubMed](#)]
159. Suzuki, H.; Araki, S.; Yamamoto, H. Evaluation of Advanced Oxidation Processes (AOP) Using  $\text{O}_3$ , UV, and  $\text{TiO}_2$  for the Degradation of Phenol in Water. *J. Water Process. Eng.* **2015**, *7*, 54–60. [[CrossRef](#)]
160. Moellmann, J.; Ehrlich, S.; Tonner, R.; Grimme, S. A DFT-D Study of Structural and Energetic Properties of  $\text{TiO}_2$  Modifications. *J. Phys. Condens. Matter.* **2012**, *24*, 424206. [[CrossRef](#)] [[PubMed](#)]
161. Scanlon, D.O.; Dunnill, C.W.; Buckeridge, J.; Shevlin, S.A.; Logsdail, A.J.; Woodley, S.M.; Catlow, C.R.A.; Powell Michael, J.; Palgrave, R.G.; Parkin, I.P.; et al. Band Alignment of Rutile and Anatase  $\text{TiO}_2$ . *Nat. Mater.* **2013**, *12*, 798–801. [[CrossRef](#)]
162. Graça, M.P.F.; Nico, C.; Peres, M.; Valente, M.A.; Monteiro, T. Study of the Optical and Dielectric Properties of  $\text{TiO}_2$  Nanocrystals Prepared by the Pechini Method. *J. Nanosci. Nanotechnol.* **2012**, *12*, 8600–8606. [[CrossRef](#)]
163. Habila, M.A.; AlOthman, Z.A.; El-Toni, A.M.; Labis, J.P.; Soyak, M. Synthesis and Application of  $\text{Fe}_3\text{O}_4$ @ $\text{SiO}_2$ @ $\text{TiO}_2$  for Photocatalytic Decomposition of Organic Matrix Simultaneously with Magnetic Solid Phase Extraction of Heavy Metals Prior to ICP-MS Analysis. *Talanta* **2016**, *154*, 539–547. [[CrossRef](#)]
164. Wilson, M.; Cheng, C.Y.C.; Oswald, G.; Srivastava, R.; Beaumont, S.K.; Badyal, J.P.S. Magnetic Recyclable Microcomposite Silica-Steel Core with  $\text{TiO}_2$  Nanocomposite Shell Photocatalysts for Sustainable Water Purification. *Colloids Surf. A Physicochem. Eng. Asp.* **2017**, *523*, 27–37. [[CrossRef](#)]
165. Chung, I.-M.; Park, I.; Seung-Hyun, K.; Thiruvengadam, M.; Rajakumar, G. Plant-Mediated Synthesis of Silver Nanoparticles: Their Characteristic Properties and Therapeutic Applications. *Nanoscale Res. Lett.* **2016**, *11*, 40. [[CrossRef](#)]
166. Ravikumar, P.; Kumar, S.S. Antifungal activity of extracellularly synthesized silver nanoparticles from *Morinda citrifolia*. *Int. J. Tech. Res. Appl.* **2014**, *2*, 108–111.

167. Inbathamizh, L.; Ponnu, T.M.; Mary, E.J. In Vitro Evaluation of Antioxidant and Anticancer Potential of Morinda Pubescens Synthesized Silver Nanoparticles. *J. Pharm. Res.* **2013**, *6*, 32–38. [[CrossRef](#)]
168. He, Z.; Cai, Q.; Fang, H.; Situ, G.; Qiu, J.; Song, S.; Chen, J. Photocatalytic Activity of TiO<sub>2</sub> Containing Anatase Nanoparticles and Rutile Nanoflower Structure Consisting of Nanorods. *J. Environ. Sci.* **2013**, *25*, 2460–2468. [[CrossRef](#)] [[PubMed](#)]
169. Hooshmand, S.; Kargozar, S.; Ghorbani, A.; Darroudi, M.; Keshavarz, M.; Bairo, F.; Kim, H.-W. Biomedical Waste Management by Using Nanophotocatalysts: The Need for New Options. *Materials* **2020**, *13*, 3511. [[CrossRef](#)] [[PubMed](#)]
170. Vimbela, G.V.; Ngo, S.M.; Frazee, C.; Yang, L.; Stout, D.A. Antibacterial properties and toxicity from metallic nanomaterials. *Int. J. Nanomed.* **2017**, *12*, 3941–3965. [[CrossRef](#)] [[PubMed](#)]
171. Verdier, T.; Coutand, M.; Bertron, A.; Roques, C. Antibacterial Activity of TiO<sub>2</sub> Photocatalyst Alone or in Coatings on *E. Coli*: The Influence of Methodological Aspects. *Coatings* **2014**, *4*, 670–686. [[CrossRef](#)]
172. Xie, J.; Hung, Y.-C. Methodology to Evaluate the Antimicrobial Effectiveness of UV-Activated TiO<sub>2</sub> Nanoparticle-Embedded Cellulose Acetate Film. *Food Control* **2019**, *106*, 106690. [[CrossRef](#)]
173. Reddy, A.K.; Kambalyal, P.B.; Shanmugasundaram, K.; Rajesh, V.; Donthula, S.; Patil, S.R. Comparative Evaluation of Antimicrobial Efficacy of Silver, Titanium Dioxide and Zinc Oxide Nanoparticles against Streptococcus Mutans. *Pesqui. Bras. Odontopediatria Clín. Integr.* **2018**, *18*, e4150. [[CrossRef](#)]
174. Long, M.; Wang, J.; Zhuang, H.; Zhang, Y.; Wu, H.; Zhang, J. Performance and Mechanism of Standard Nano-TiO<sub>2</sub> (P-25) in Photocatalytic Disinfection of Foodborne Microorganisms—Salmonella Typhimurium and Listeria Monocytogenes. *Food Control* **2014**, *39*, 68–74. [[CrossRef](#)]
175. Altın, İ.; Sökmen, M. Preparation of TiO<sub>2</sub>-Polystyrene Photocatalyst from Waste Material and Its Usability for Removal of Various Pollutants. *Appl. Catal. B Environ.* **2014**, *144*, 694–701. [[CrossRef](#)]
176. Bonetta, S.; Bonetta, S.; Motta, F.; Strini, A.; Carraro, E. Photocatalytic Bacterial Inactivation by TiO<sub>2</sub>-Coated Surfaces. *AMB Expr.* **2013**, *3*, 59. [[CrossRef](#)]
177. Yao, N.; Lun Yeung, K. Investigation of the Performance of TiO<sub>2</sub> Photocatalytic Coatings. *Chem. Eng. J.* **2011**, *167*, 13–21. [[CrossRef](#)] [[PubMed](#)]
178. Luo, Z.S.; Ye, Q.Y.; Li, D.D. Influence of nano-TiO<sub>2</sub> modified LDPE film packaging on quality of strawberry. *Mod. Food Sci. Technol.* **2013**, *29*, 2340–2344.
179. Gumiero, M.; Peressini, D.; Pizzariello, A.; Sensidoni, A.; Iacumin, L.; Comi, G.; Toniolo, R. Effect of TiO<sub>2</sub> Photocatalytic Activity in a HDPE-Based Food Packaging on the Structural and Microbiological Stability of a Short-Ripened Cheese. *Food Chem.* **2013**, *138*, 1633–1640. [[CrossRef](#)] [[PubMed](#)]
180. Wang, J.; Li, C.; Zhuang, H.; Zhang, J. Photocatalytic Degradation of Methylene Blue and Inactivation of Gram-Negative Bacteria by TiO<sub>2</sub> Nanoparticles in Aqueous Suspension. *Food Control* **2013**, *34*, 372–377. [[CrossRef](#)]
181. Yue, Q.; Sun, J.; Kang, Y.; Deng, Y. Advances in the Interfacial Assembly of Mesoporous Silica on Magnetite Particles. *Angew. Chem. Int. Ed.* **2020**, *59*, 15804–15817. [[CrossRef](#)] [[PubMed](#)]
182. Liang, J.; Liang, Z.; Zou, R.; Zhao, Y. Heterogeneous Catalysis in Zeolites, Mesoporous Silica, and Metal-Organic Frameworks. *Adv. Mater.* **2017**, *29*, 1701139. [[CrossRef](#)] [[PubMed](#)]
183. Fujiwara, K.; Kuwahara, Y.; Sumida, Y.; Yamashita, H. Fabrication of Photocatalytic Paper Using TiO<sub>2</sub> Nanoparticles Confined in Hollow Silica Capsules. *Langmuir* **2017**, *33*, 288–295. [[CrossRef](#)]
184. Wang, D.; Han, D.; Shi, Z.; Wang, J.; Yang, J.; Li, X.; Song, H. Optimized Design of Three-Dimensional Multi-Shell Fe<sub>3</sub>O<sub>4</sub>/SiO<sub>2</sub>/ZnO/ZnSe Microspheres with Type II Heterostructure for Photocatalytic Applications. *Appl. Catal. B Environ.* **2018**, *227*, 61–69. [[CrossRef](#)]
185. Tang, X.; Feng, Q.; Liu, K.; Luo, X.; Huang, J.; Li, Z. A simple and innovative route to remarkably enhance the photocatalytic performance of TiO<sub>2</sub>: Using micro-meso porous silica nanofibers as carrier to support highly-dispersed TiO<sub>2</sub> nanoparticles. *Micropor. Mesopor. Mater.* **2018**, *258*, 251–261. [[CrossRef](#)]
186. Mohanty, S.; Babu, P.; Parida, K.; Naik, B. Surface-Plasmon-Resonance-Induced Photocatalysis by Core-Shell SiO<sub>2</sub>@Ag NCs@Ag<sub>3</sub>PO<sub>4</sub> toward Water-Splitting and Phenol Oxidation Reactions. *Inorg. Chem.* **2019**, *58*, 9643–9654. [[CrossRef](#)]
187. Singh, R.; Bapat, R.; Qin, L.; Feng, H.; Polshettiwar, V. Atomic Layer Deposited (ALD) TiO<sub>2</sub> on Fibrous Nano-Silica (KCC-1) for Photocatalysis: Nanoparticle Formation and Size Quantization Effect. *ACS Catal.* **2016**, *6*, 2770–2784. [[CrossRef](#)]
188. Yin, Q.; Wu, W.; Qiao, R.; Ke, X.; Hu, Y.; Li, Z. Glucose-Assisted Transformation of Ni-Doped-ZnO@carbon to a Ni-Doped-ZnO@void@SiO<sub>2</sub> Core-Shell Nanocomposite Photocatalyst. *RSC Adv.* **2016**, *6*, 38653–38661. [[CrossRef](#)]
189. Zhang, X.; Huang, H.; Liu, J.; Liu, Y.; Kang, Z. Carbon Quantum Dots Serving as Spectral Converters through Broadband Upconversion of Near-Infrared Photons for Photoelectrochemical Hydrogen Generation. *J. Mater. Chem. A* **2013**, *1*, 11529. [[CrossRef](#)]
190. Rajendiran, K.; Zhao, Z.; Pei, D.-S.; Fu, A. Antimicrobial Activity and Mechanism of Functionalized Quantum Dots. *Polymers* **2019**, *11*, 1670. [[CrossRef](#)]
191. Moradlou, O.; Rabiei, Z.; Banazadeh, A.; Warzywoda, J.; Zirak, M. Carbon Quantum Dots as Nano-Scaffolds for  $\alpha$ -Fe<sub>2</sub>O<sub>3</sub> Growth: Preparation of Ti/CQD@ $\alpha$ -Fe<sub>2</sub>O<sub>3</sub> Photoanode for Water Splitting under Visible Light Irradiation. *Appl. Catal. B Environ.* **2018**, *227*, 178–189. [[CrossRef](#)]

192. Lops, C.; Ancona, A.; Di Cesare, K.; Dumontel, B.; Garino, N.; Canavese, G.; Hernández, S.; Cauda, V. Sonophotocatalytic Degradation Mechanisms of Rhodamine B Dye via Radicals Generation by Micro-and Nano-Particles of ZnO. *Appl. Catal. B Environ.* **2019**, *243*, 629–640. [CrossRef]
193. Madhav, S.; Ahamad, A.; Singh, P.; Mishra, P.K. A Review of Textile Industry: Wet Processing, Environmental Impacts, and Effluent Treatment Methods. *Environ. Qual. Manag.* **2018**, *27*, 31–41. [CrossRef]
194. Wang, S.; Xu, M.; Peng, T.; Zhang, C.; Li, T.; Hussain, I.; Wang, J.; Tan, B. Porous Hypercrosslinked Polymer-TiO<sub>2</sub>-Graphene Composite Photocatalysts for Visible-Light-Driven CO<sub>2</sub> Conversion. *Nat. Commun.* **2019**, *10*, 676. [CrossRef]
195. Tang, Y.; Zhou, P.; Wang, K.; Lin, F.; Lai, J.; Chao, Y.; Li, H.; Guo, S. BiOCl/Ultrathin Polyaniline Core/Shell Nanosheets with a Sensitization Mechanism for Efficient Visible-Light-Driven Photocatalysis. *Sci. China Mater.* **2019**, *62*, 95–102. [CrossRef]
196. Fu, J.; Yu, J.; Jiang, C.; Cheng, B. G-C<sub>3</sub>N<sub>4</sub>-Based Heterostructured Photocatalysts. *Adv. Energy Mater.* **2018**, *8*, 1701503. [CrossRef]
197. Zhang, X.; Wei, W.; Zhang, S.; Wen, B.; Su, Z. Advanced 3D Nanohybrid Foam Based on Graphene Oxide: Facile Fabrication Strategy, Interfacial Synergetic Mechanism, and Excellent Photocatalytic Performance. *Sci. China Mater.* **2019**, *62*, 1888–1897. [CrossRef]
198. Chen, S.; Yu, J.; Zhang, J. Enhanced Photocatalytic CO<sub>2</sub> Reduction Activity of MOF-Derived ZnO/NiO Porous Hollow Spheres. *J. CO<sub>2</sub> Util.* **2018**, *24*, 548–554. [CrossRef]
199. Teimouri, M.; Husain, S.W.; Saber-Tehrani, M.; Aberoomand-Azar, P. Preparation of Novel Ni/Co Co-Doping Fe<sub>3</sub>O<sub>4</sub>/TiO<sub>2</sub> Core-Shell Nanocomposites and Their Use in Effective Photocatalytic Degradation of Amlodipine Drug. *Sep. Sci. Technol.* **2019**, *54*, 634–641. [CrossRef]
200. Stefan, M.; Leostean, C.; Pana, O.; Toloman, D.; Popa, A.; Perhaita, I.; Senilă, M.; Marincas, O.; Barbu-Tudoran, L. Magnetic Recoverable Fe<sub>3</sub>O<sub>4</sub>-TiO<sub>2</sub>:Eu Composite Nanoparticles with Enhanced Photocatalytic Activity. *Appl. Surf. Sci.* **2016**, *390*, 248–259. [CrossRef]
201. Abbas, M.; Rao, B.P.; Reddy, V.; Kim, C. Fe<sub>3</sub>O<sub>4</sub>/TiO<sub>2</sub> Core/Shell Nanocubes: Single-Batch Surfactantless Synthesis, Characterization and Efficient Catalysts for Methylene Blue Degradation. *Ceram. Int.* **2014**, *40*, 11177–11186. [CrossRef]
202. Golshan, M.; Kakavandi, B.; Ahmadi, M.; Azizi, M. Photocatalytic Activation of Peroxymonosulfate by TiO<sub>2</sub> Anchored on Copper Ferrite (TiO<sub>2</sub>@CuFe<sub>2</sub>O<sub>4</sub>) into 2,4-D Degradation: Process Feasibility, Mechanism and Pathway. *J. Hazard. Mater.* **2018**, *359*, 325–337. [CrossRef]
203. Dung, N.T. Preparation of Magnetic Antibacterial Composite Beads Fe<sub>3</sub>O<sub>4</sub>/Alginate/Ag. *Vietnam. J. Sci. Technol.* **2018**, *56*, 192. [CrossRef]
204. Moosavi, S.M.; Molla-Abbasi, P.; Haji-Aghajani, Z. Photo-Catalyst CoFe<sub>2</sub>O<sub>4</sub>-TiO<sub>2</sub>: Application in Photo-Degradation of Organic Dyes and Magnetic Nanocomposite Preparation. *J. Mater. Sci. Mater. Electron.* **2016**, *27*, 4879–4886. [CrossRef]
205. Bavarsih, F.; Rajabi, M.; Montazeri-Pour, M. Synthesis of SrFe<sub>12</sub>O<sub>19</sub>/SiO<sub>2</sub>/TiO<sub>2</sub> Composites with Core/Shell/Shell Nano-Structure and Evaluation of Their Photo-Catalytic Efficiency for Degradation of Methylene Blue. *J. Mater. Sci. Mater. Electron.* **2018**, *29*, 1877–1887. [CrossRef]
206. Chen, C.-C.; Fu, Y.-P.; Hu, S.-H. Characterizations of TiO<sub>2</sub>/SiO<sub>2</sub>/Ni-Cu-Zn Ferrite Composite for Magnetic Photocatalysts. *J. Am. Ceram. Soc.* **2015**, *98*, 2803–2811. [CrossRef]
207. Coromelci, C.; Neamtu, M.; Ignat, M.; Samoila, P.; Zaltariov, M.F.; Palamaru, M. Ultrasound Assisted Synthesis of Heterostructured TiO<sub>2</sub>/ZnFe<sub>2</sub>O<sub>4</sub> and TiO<sub>2</sub>/ZnFe<sub>1.98</sub>La<sub>0.02</sub>O<sub>4</sub> Systems as Tunable Photocatalysts for Efficient Organic Pollutants Removal. *Ceram. Int.* **2022**, *48*, 4829–4840. [CrossRef]
208. Mandal, S.; Adhikari, S.; Pu, S.; Wang, X.; Kim, D.-H.; Patel, R.K. Interactive Fe<sub>2</sub>O<sub>3</sub>/Porous SiO<sub>2</sub> Nanospheres for Photocatalytic Degradation of Organic Pollutants: Kinetic and Mechanistic Approach. *Chemosphere* **2019**, *234*, 596–607. [CrossRef] [PubMed]
209. Grewal, J.K.; Kaur, M.; Sharma, R.K.; Oliveira, A.C.; Garg, V.K.; Sharma, V.K. Structural and Photocatalytic Studies on Oxygen Hyperstoichiometric Titanium-Substituted Strontium Ferrite Nanoparticles. *Magnetochemistry* **2022**, *8*, 120. [CrossRef]
210. Singh, G.; Kaur, M.; Kumar Garg, V.; Oliveira, A.C. Oxygen Hyper Stoichiometric Trimetallic Titanium Doped Magnesium Ferrite: Structural and Photocatalytic Studies. *Ceram. Int.* **2022**, *48*, 24476–24484. [CrossRef]
211. Grewal, J.K.; Kaur, M.; Ubhi, M.K.; Oliveira, A.C.; Garg, V.K.; Sharma, V.K. Structural, Magnetic, and Photocatalytic Properties of Core-Shell Reversal Nanocomposites of Titanium-Doped Strontium Ferrite and Silica. *J. Mater. Res.* **2023**, *38*, 1019–1034. [CrossRef]
212. Redfield, R.R. Antibiotic Resistance Threats in the United States. (U.S. Centers for Disease Control and Prevention). *Am. Fam. Physician* **2014**, *89*, 938–941. [CrossRef]
213. O'Neill, J. *Tackling Drug-Resistant Infections Globally: Final Report and Recommendations*. London: Review on Antimicrobial Resistance; Government of United Kingdom: London, UK, 2016; pp. 1–84.
214. Chen, W.-J.; Tsai, P.-J.; Chen, Y.-C. Functional Fe<sub>3</sub>O<sub>4</sub>/TiO<sub>2</sub> Core/Shell Magnetic Nanoparticles as Photokilling Agents for Pathogenic Bacteria. *Small* **2008**, *4*, 485–491. [CrossRef]
215. Cui, B.; Peng, H.; Xia, H.; Guo, X.; Guo, H. Magnetically Recoverable Core-Shell Nanocomposites  $\gamma$ -Fe<sub>2</sub>O<sub>3</sub>@SiO<sub>2</sub>@TiO<sub>2</sub>-Ag with Enhanced Photocatalytic Activity and Antibacterial Activity. *Separ. Purif. Technol.* **2013**, *103*, 251–257. [CrossRef]
216. Yang, J.; Gao, G.; Zhang, X.; Ma, Y.-H.; Chen, X.; Wu, F.-G. One-Step Synthesis of Carbon Dots with Bacterial Contact-Enhanced Fluorescence Emission: Fast Gram-Type Identification and Selective Gram-Positive Bacterial Inactivation. *Carbon* **2019**, *146*, 827–839. [CrossRef]

217. Moradlou, O.; Rabiei, Z.; Delavari, N. Antibacterial Effects of Carbon Quantum Dots@hematite Nanostructures Deposited on Titanium against Gram-Positive and Gram-Negative Bacteria. *J. Photochem. Photobiol. A Chem.* **2019**, *379*, 144–149. [[CrossRef](#)]
218. Kooti, M.; Gharineh, S.; Mehrkhah, M.; Shaker, A.; Motamedi, H. Preparation and Antibacterial Activity of CoFe<sub>2</sub>O<sub>4</sub>/SiO<sub>2</sub>/Ag Composite Impregnated with Streptomycin. *Chem. Eng. J.* **2015**, *259*, 34–42. [[CrossRef](#)]

**Disclaimer/Publisher's Note:** The statements, opinions and data contained in all publications are solely those of the individual author(s) and contributor(s) and not of MDPI and/or the editor(s). MDPI and/or the editor(s) disclaim responsibility for any injury to people or property resulting from any ideas, methods, instructions or products referred to in the content.